NASA-CR-178152

IMPLEMENTATION OF AND MEASUREMENT WITH
THE LIPA TECHNIQUE IN A SUBSONIC JET

/00 50
75 P

R. E. Falco

Final Report
NASA Grant NAG-3-1091

Michigan State University
Department of Mechanical Engineering
East Lansing, MI 48824

August 1994

Standard Bibliographic Page

1. Report No. NASA CR-178152	2. Government Accession No.	3. Recipient's Catalog No.
4. Title and Subtitle Implementation of and Measurement with the LIPA technique in a subsonic jet		5. Report Date **September 1987**
		6. Performing Organization Code TSL-94-2
7. Author(s) R. E. Falco		8. Performing Organization Report No.
9. Performing Organization Name and Address Michigan State University Turbulence Structure Laboratory Department of Mechanical Engineering East Lansing, MI 48824		10. Work Unit No. 505-60-31-04
		11. Contract or Grant No. NAG-3-1091
12. Sponsoring Agency Name and Address National Aeronautics and Space Administration Washington, DC 20546		13. Type of Report and Period Covered Final
		14. Sponsoring Agency Code

15. Supplementary Notes

16. Abstract

LIPA (Laser Induced Photochemical Anemometry) was used to measure velocity, vorticity, Reynolds stress and turbulent intensity distributions in a subsonic jet. The jet region of interest was the area close to the jet-orifice. The LIPA-technique is a non-intrusive quantitative flow visualization technique, consisting of tracking a phosphorescing grid of fluid particles, which is impressed by laser-beams directed into the flow. The phosphorescence of biacetyl gas was used to enable tracking of the impressed light grid. In order to perform measurements in a jet, LIPA was developed and implemented for the specific flow requirements. Nitrogen was used as the carrier gas to avoid quenching of the phosphorescent radiation of the tracer gas biacetyl by ambient oxygen. The use of sulfur dioxide to sensitize phosphorescent emission of biacetyl was examined. Preliminary data was used in a discussion of the potential of the LIPA-technique.

17. Key Words (Suggested by Authors(s)) LIPA Jet whole field	18. Distribution Statement Unclassified – unlimited Subject Category 34	
19. Security Classif.(of this report) Unclassified	20. Security Classif.(of this page) Unclassified	21. No. of Pages	22. Price A10

NASA   Form 63 (June 1985)

ABSTRACT

IMPLEMENTATION OF AND MEASUREMENT WITH
THE LIPA-TECHNIQUE IN A SUBSONIC JET

LIPA (Laser Induced Photochemical Anemometry) was used to measure velocity, vorticity, Reynolds stress and turbulent intensity distributions in a subsonic jet. The jet region of interest was the area close to the jet-orifice. The LIPA-technique is a non-intrusive quantitative flow visualization technique, consisting of tracking a phosphorescing grid of fluid particles, which is impressed by laser-beams directed into the flow. The phosphorescence of biacetyl gas was used to enable tracking of the impressed light grid. In order to perform measurements in a jet, LIPA was developed and implemented for the specific flow requirements. Nitrogen was used as the carrier gas to avoid quenching of the phosphorescent radiation of the tracer gas biacetyl by ambient oxygen. The use of sulfur dioxide to sensitize phosphorescent emission of biacetyl was examined. Preliminary data was used in a discussion of the potential of the LIPA-technique.

TABLE OF CONTENTS

LIST OF SYMBOLS

<u>Roman</u>

A	Area
Ac_2	Biacetyl
C	Circumference
C_1, C_2	Proportionality constants
CR	Confidence region
E	Energy
E_t	Triplet energy
FDC	Fluid dynamic quantaties
f	Focus length
I	Intensity
I_e	Intensity of emission
I_f	Intensity of fluorescence emission
I_p	Intensity of phosphorescence emission
I_l	Intensity of laser line energy
k	Rate constant
l_d	Diffusion length
m	Grid mesh size
p	Pressure
r	Jet exit nozzle radius
RCR	Relative confidence region
rms	Root mean square
RSE	Relative standart error
S	Path along which circulation is calculated (circumference of a grid box)
SE	Standard error
s	Distance of movement of grid intersection points
t	t-factor (see error analysis)
u	Fluctuating part of streamwise local velocity
u'	Root mean square of u
U	Local mean velocity
U_c	Core velocity
v	Fluctuating part of normal local velocity
v'	Root mean square of v
x	Streamwise Cartesian coordinate

x_l	Coordinate along laserbeam
y	Normal Cartesian coordinate

Greek

α	Absorption coefficient
Γ	Circulation
ε	Extinction coefficient
Φ_p	Phosphorescent quantum yield (emitted intensity/absorbed intensity)
Δt	Time interval between laser pulse and picture detection
Δt_l	Time interval between laser trigger out TTL-signal and actual laser pulse
τ_e	Emission lifetime
τ_f	Fluorescent lifetime
τ_p	Phosphorescent lifetime
ω_z	Vorticity component perpendicular to grid plane
ξ_e	Observed emission length in streamwise direction (still camera experiments)

Superscripts

'	Indicates relation to 'reference grid'
"	Indicates relation to 'distorted grid'
1	Indicates singlet state
3	Indicates triplet state

Other

[ ]	Indicates mol-density (mol/volume)
⎯	Mean value of local quantity
< >	Mean value of local quantity (same as overbar)

1. Introduction

Optical techniques are widely used in fluid mechanics to observe and measure properties of flow fields such as velocities and densities. Many of these techniques are qualitative but of great value in guiding intuition for further research by quantitative means. Optical techniques are usually known for their largely nonintrusive properties as compared with methods like the Pitot tube or the hot-wire technique.

Flow-visualization techniques may be coarsely subdivided into two categories: those that make use of light scattered by tiny particles in the fluid and those that make use of variation in fluid properties (i. e. refractive index). Among the methods that rely on scattered light, laser Doppler anemometry is now a standard means of obtaining fluid velocities. In laser Doppler anemometry, the fluid velocity can be measured with high accuracy as a function of time but only at a single point in the fluid at any given time. Particle Image Velocimetry (PIV) has been developed to enable researchers to look at instantaneous spatial data. The ultimate aim, of course, is the simultaneous determination of fluid velocities in a whole volume of a fluid. First steps in this direction have been taken with the development of speckle photography, which can give the instantaneous velocity field over a complete plane of interest in a fluid. Among the methods that make use of refractive index variation, holographic methods are established. All of the above techniques require the use of particles in the flow.

LIPA (Laser Induced Photochemical Anemometry) has been recently developed and has the ability of simultaneous determination of fluid dynamic quantities like velocity over a whole volume of a fluid. This technique makes use of excited luminescent particles or molecules, thus, special seed molecules have to be introduced into the flow as the normal lifetime of the excited states is not long enough with respect to the time scale of the flow. Such molecules are the key component of the LIPA measuring technique.

LIPA can also be performed for liquid flows using photochromic dyes or luminescent particles, which are premixed with the fluid and excited by a laser at specific locations in the test section. Due to the low vapor pressure of photochromic dyes, and the static charge that builds up in luminescence particles, these laser-marking methods are

not well suited for gas flows. One way to mark fluid elements in gases in a similar fashion as done with liquids would be to use laser-induced phosphorescence. In contrast with fluorescence, which involves quantum-allowed transitions and short lifetimes $(10^{-6}$-10^{-8}s$)$, phosphorescence occurs via forbidden transitions and, therefore, has a long radiative lifetime $(>10^{-4}$s$)$.

LIPA was previously conducted successfully in media such as water and kerosene [1,2] where luminescent chemicals can be dissolved easily. Tests in a Mach 3 jet gas flow [3] showed the potential for the LIPA investigation of a jet flow, however, no calibrated data was obtained. The jet was seeded with droplets of a water diluted luminescent chemical. The first successful LIPA investigation of a gas flow field has been made recently in a motored two-stroke engine during scavenging [4].

Biacetyl vapor, the luminescent chemical that is used in the present investigation, was first introduced as a flow field diagnostic material by Epstein [5] who made use of the fluorescence of biacetyl. Whereas biacetyls fluorescence has been used later on by McKenzie [6], Hiller [7] and Hilbert [4] applied biacetyls phosphorescence to flow field diagnostic. Because biacetyls phosphorescence, in contrast to its fluorescence, is strongly quenched by oxygen, the latter implementations have been made with nitrogen-biacetyl gas mixtures.

There have been a large number of investigations of turbulent jets mainly because of their engineering importance, simplicity and relevance to other turbulent flows. Two books have been published which are largely devoted to this subject (see references [8] and [9]). Most experimental velocity measurements in turbulent jets have been made with hot-wire instrumentation. However, other studies have recently been performed using laser-Doppler velocimetry (LDV). Studies in supersonic jets are more difficult, because probes interfere with the shock structure. The particles needed for LDA may also cause problems. Therefore, LIPA, as developed here, may one day be a powerful tool for supersonic jet research.

A general jet flow may be separated into three regions, each having a distinctly different character. One region consists of a potential core of uniform mean velocity and

low intensity of turbulent fluctuations bounded by a shear layer. This region starts at the nozzle exit and has a length of 4 or 5 nozzle diameters. The mixing region, which lies between the central core and the undisturbed gas of the surroundings, where the velocity gradients are large and the intensity of turbulence is high, is a second region. The third region, where the central core and the mixing region blend into a completely turbulent gasstream starts at about 8 nozzle diameter behind the nozzle exit.
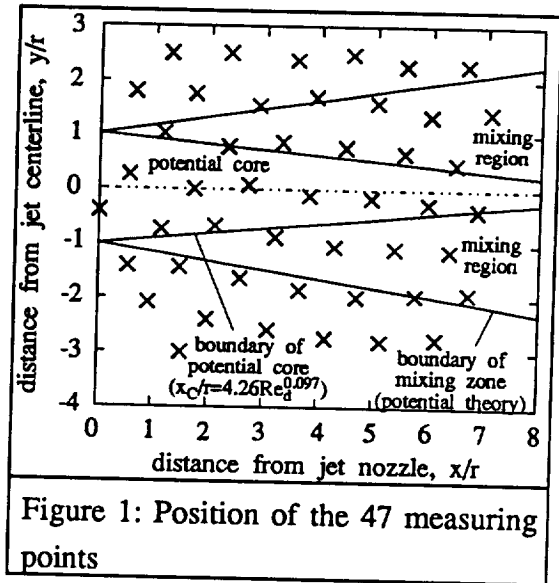
Figure 1: Position of the 47 measuring points

In this work LIPA is applied in an axial symmetrical round jet of a nitrogen-biacetyl gas mixture. The diameter of the jet exit nozzle is 10mm and the Reynolds number (based on the inner orifice diameter) of the room temperature (20°C) jet flow is about 12400. The 47 measuring points employed here (see figure 1) cover an area of a approximate distance from the jet centerline $\pm 3r$ and a distance from the jet nozzle in streamwise direction of 0 to $7r$. According to the estimated boundary of the potential core with Harshas correlation (see [10], pg.: 20) and of the mixing zone with the potential theory, 23 measuring points lie in gas of the surroundings, 14 measuring points are in the mixing area and 10 measuring points are in the area of the potential core.

2. Experimental set-up

A typical LIPA experimental set-up consists of three main components. One is the flow creation, which includes the seeding, if necessary, of the carrier gas with the luminescent chemical and the devices to generate the flow field of interest. A second element creates the light beam grid and consists of a pulsed light source (usually a pulsed laser), mirrors, lenses and a beam splitter to direct the light to the measurement area and beam dividers to create a grid pattern. A third component, that detects and stores the grid patterns (commonly a movie, CCD or CID camera with controllable shutter timing, which stores the detected information on a media like regular film material, video tape or disk), has to be, either case, coupled with the light-source to control the delay time between light pulse and detection.

The chosen set-up for the LIPA-implication for measurements in a free jet is schematically shown in figure 4.

The light source is a Lambda Physiks LPX 220 pulsed excimer laser. It is charged with XeCl gas and the buffer-gas is neon. It emits ultra violet light at 308 nm. The initial beam size is about 5 mm by 20 mm and the maximum pulse energy that can be emitted during a pulse-length of 20 ns is 220 mJ. The maximum pulse energy decreases with increase of the pulse repetition rate, that can be controlled internally (up to 100 pulses/second) or externally (up to 250 pulses/second). The laser beam is directed by broad band aluminum coated mirrors and a 50:50 308nm dielectrically coated beam splitter through bi-convex quartz lenses of a focal length of 300mm to the beam dividers in order to create a grid of laser beams in the jet area of interest. The average pulse energy carried by one grid beam is determined to be about 3% of the initial pulse energy, whereas a grid beam diameter (without scattering by the flow) of about 0.5 mm is detected.

The implementation of the LIPA-technique requires 'lines' of laser light to create a grid pattern. A beam divider is used to create several beams from one initial beam. In order to lose as little light as possible a beam divider that is shown schematically in figure 2 is employed. The design of the beam divider resembles an oversized blazed reflec-

tion grating. Apart from diffraction and absorption effects, it provides no loss of incident laser energy if the angle between the incident beam and the metal base (φ) is adjusted properly. Since the applied broad-band excimer laser radiation shows only a low degree of coherence, additional diffraction patterns (which could be observed if HeNe laser light was used for the irradiation) are absent so that the grid

Figure 2: Beam divider to create parallel beams (specular reflection) from one incident beam

of beams in the test area is well defined. The aluminium coating of the mirrors is optimized for shallow incidence angles. Mesh sizes of 4.2 mm to 5.2 mm are generated in the actual experiment.

The flowfield is generated by a 17m/s nitrogen jet (nozzle exit diameter: 1 cm) seeded with approximately 5 mol% biacetyl, issuing into a 12 cm diameter and 74 cm long plexiglass tube. A slow side jet of the same gas mixture is provided to prevent self-feeding of the main jet. Quartz plexiglass windows are fitted into the tube to let the laser beams pass through and a honeycomb in the tube exit

Figure 3: Gas-dispersion bottle

create a pressure gradient in order to reduce incoming oxygen and hence quenching of biacetyl emission by oxygen. The tank, that is connected to the exit nozzle, is provided with honeycombs (see appendix F) in order to reduce swirls in the initial jet. Seeding of the jet fluid with biacetyl (liquid at room temperature and atmosphere pressure) is accomplished by room temperature gas-dispersion (see figure 3). Nitrogen of 99.995% purity, provided by an industrial gas tank and pressure reduced by an industrial regulator, is dispersed through liquid biacetyl in a mixing chamber to evaporate biacetyl. To disperse the nitrogen through the biacetyl, a open ended tube is chosen in order to reduce the pressure in the nitrogen delivery system [11].
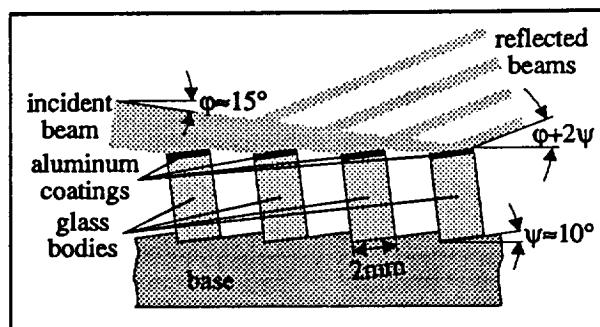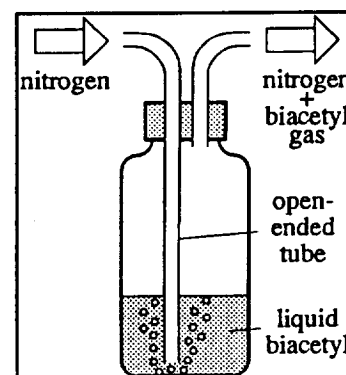
A gated ICCD (intensified charge coupled device) camera (ICCD-576 manufactured by Princeton Instruments) is applied to detect the grid patterns. Its detector (Thomson-CSF TH7883FO-2: 576 columns x 384 rows; spectral range of 400-1060nm sensitivity; dynamic range of 14-bits) is operated by a detector controller (Princeton Instruments ST-130) that interfaces to a personal computer (Dell 325D). The camera is equipped with a 58mm lens (f-stop: 1:1.2) and a 52mm close-up lens. This optical set-up provides for the picture area a resolution of 0.0735 mm/pixel. The excimer-laser is the source of the system trigger. Two pulse generators are employed to set the delay between the laser pulse and the picture detection. Pulse generator #1 (Princeton Instruments FG-100) controls the time delay between the excimer-laser trigger signal and the actual laser pulse ($\Delta t_l \approx 300$ns), the time duration of the gating and prevents gating through CCD readout to reduce background noise. Pulse generator #2 provides pulse generator #1 with the actual delay between laser pulse and detector gating (Δt), an additional delay on Δt_l. A second pulse generator is necessary because of the limited delay range of pulse generator #1 (20-1700 ns, whereas a delay time of $\Delta t = 30$ to 90µs is required). A two channel oscilloscope is used to display and measure the time delays.

Two types of datagrids are taken; undistorted and distorted grids. The undistorted grids are captured when the laser is firing, whereas the distorted grids are captured at a specified time delay after the laser pulse. Because of the low image detection repetition rate of the camera assembly (about 3 pictures/minutes), the distorted and undistorted grids are detected in different events (not during the same illumination process). Since indeed the undistorted grid pattern is detected at the time of the laser pulse, it is created by straight lines, and hence fundamentally a reference grid for all the distorted grids that are taken with the same experimental set-up.

The camera assembly stores the raw data (pictures) on the hard drive of the personal computer. In order to download the data sets into a Megavision 1024 XM image processor the data has to be reformatted to a 8-bit 512x512 pixel format (512 of the original 576 columns, 8 of the original 14 bits). This is necessary, because the image processor can only read data of a certain format.
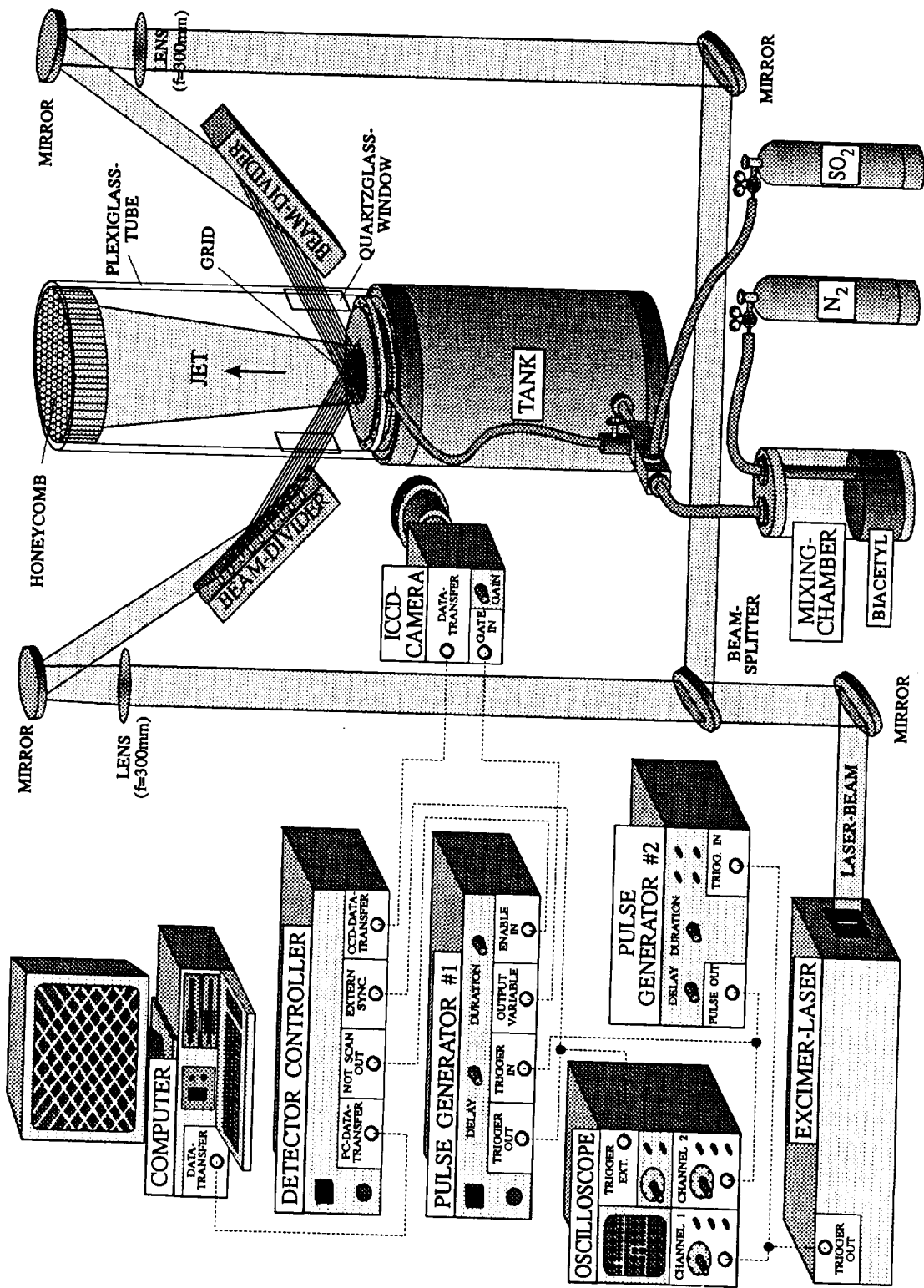
Figure 4: LIPA-experiment set-up for measurments in a jet using a ICCD-camera

3. Experimental procedure

3.1 The LIPA technique

3.1.1 Review of the measurement technique

The technique of Laser Induced Photochemical Anemometry (LIPA) makes use of exited photochromic chemicals to measure important fluid quantities such as velocity and vorticity over a two-dimensional area of a fluid flow.

Excited photochromic molecules can emit light for a certain time-interval (τ_e) after excitation. Hence, a photochromic molecules containing flow-volume irradiated by a laser pulse (pulse length $<< \tau_e$) can emit light for a certain time-interval after the laser pulse. If non intrusive, with the flow moving photochromic chemicals are used, the path of a marked flow volume can be followed during the lifetime of the impressed light emission.

The LIPA technique marks and follows points in the flow-field by employing photochromic molecules. The flow is seeded with a photochromic chemical and lines of pulsed laser light are directed into the flow. This impresses a grid of intersecting, light emitting fluid lines within the flow. The lines and especially the intersections of the lines, which define points in the flow, can be followed for a certain time after its creation.

Two successive pictures of the grid are required to obtain fluid dynamic quantities of the flow field. Separate pictures taken at the time of the laser pulse (a undeformed 'reference grid') and after a time delay shorter than the lifetime of the emission (a 'deformed grid'). By measuring the distance and direction each intersection travels and by knowing the time delay between each photograph, the two velocity components in the grid plane, turbulence intensities, Reynolds stress and vorticity can be calculated.

3.1.2 Algorithms to obtain fluid dynamic quantities

To describe the procedure to obtain fluid dynamic quantities from a 'reference grid' and a 'distorted grid', one 'grid box' is chosen (see figure 5a). If the mesh size of the grid is small enough, one box can be thought of as a fluid 'particle'.

A fluid particle moving in a general three-dimensional flow field may have motions about all three coordinate axes. The LIPA technique, in means of the application as it is shown here, is limited to the projection of a three-dimensional motion of the particle onto the plane of the photos which is parallel to the initial plane of the grid.

As a particle moves with the flow, it may undergo several motions that can translate, rotate and deform the 'grid box' in the plane of the photos. Because the history of this specific fluid particle is known, the displacement $\Delta \vec{s}_i = (x_{i''}-x_{i'}, y_{i''}-y_{i'})$ and the velocity $\vec{U}_i = \Delta \vec{s}_i / \Delta t$ of each corner i can be calculated. The latter are average velocities over the time interval Δt, thus, they are designated to an average 'grid box' (see figure 5b and figure 6: (1,2,3,4)) whose corners are positioned at the midpoint between the associated corners of the reference and distorted 'grid box' $(x_i, y_i) = ((x_{i'}+x_{i''})/2, (y_{i'}+y_{i''})/2)$.

Figure 5: Procedure for conversation of the displacement between the reference (1',2',3',4') and the distorted (1",2",3",4") 'grid box' to velocities.
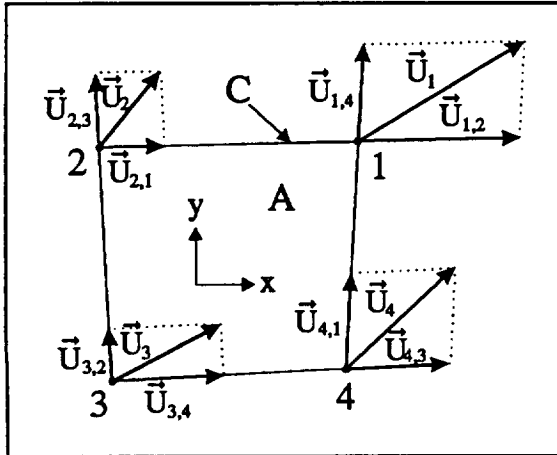
Figure 6: Decomposition of the velocities used to calculate the circulation around a 'grid box' of the area A and the circumference C.

To calculate the vorticity from the 'grid box' (1,2,3,4) and the velocities ($\vec{U}_i$) the definition of the circulation Γ is used:

$$\Gamma = \oint_C \vec{U} \bullet d\vec{S} \qquad (3.1)$$

To relate the surface integral to an area integral, Gauss' theorem is employed, and leads to:

$$\Gamma = \int_A \vec{\omega}_z \bullet \vec{n}\, dA \qquad (3.2)$$

$$\text{with:}\quad \omega_z = \frac{\partial v}{\partial x} - \frac{\partial u}{\partial y} \qquad (3.3)$$

The velocity vector at each corner is converted to the directions of the box sidelines (see figure 6). Assuming a linear change of the velocity components along the box sidelines, $\vec{U} \bullet d\vec{S}$ in equation (3.1) is estimated for every box side by forming the average of the corner velocity components in the box sideline direction:

$$\Gamma = \oint_C \vec{U} \bullet d\vec{S} = \int_1^2 \vec{U} \bullet d\vec{S} + \int_2^3 \vec{U} \bullet d\vec{S} + \int_3^4 \vec{U} \bullet d\vec{S} + \int_4^1 \vec{U} \bullet d\vec{S} \qquad (3.4)$$

$$\cong \frac{\vec{U}_{1,2}+\vec{U}_{2,1}}{2} \bullet \vec{S}_{1,2} + \frac{\vec{U}_{2,3}+\vec{U}_{3,2}}{2} \bullet \vec{S}_{2,3} + \frac{\vec{U}_{3,4}+\vec{U}_{4,3}}{2} \bullet \vec{S}_{3,4} + \frac{\vec{U}_{4,1}+\vec{U}_{1,4}}{2} \bullet \vec{S}_{4,1}$$

$$\text{with:}\quad \vec{S}_{i,j} = \begin{pmatrix} x_j - x_i \\ y_j - y_i \end{pmatrix}$$

The average vorticity component at the centroid of the fluid particle normal to the picture plane ω_z can be obtained by dividing the calculated circulation Γ by the area A of the fluid particle (equation 3.2):

$$\omega_z = \frac{\Gamma}{A} \qquad (3.5)$$

This technique has the advantages of avoiding a second differencing of the experiment data.

By following this procedure for the other mesh elements, the vorticity components normal to the picture plane, and though in the plane of the initial grid, can be obtained at many locations over a two-dimensional field in a flow simultaneously.

<u>3.1.3 Error analysis</u>

An error analysis, which indicates the expected relative error associated with the fluid dynamic quantities is shown. This error analysis is based on the assumption, that errors are generated only by inaccurate evaluation of the position of the grid intersection points. Other possible errors origins are neglected in this analysis.

Assume that there is a uncertainty of the evaluated position of an intersection point (reference grid: $\delta s'$; distorted grid: $\delta s''$) that moves a distance Δs during a time interval Δt. The expected errors for the single local measurement (single intersection point of single grid) are calculated as [12,13]:

local velocity:

$$\delta U_x = \delta U_y = \delta u = \delta v = \frac{\sqrt{(\delta s')^2 + (\delta s'')^2}}{\Delta t} \qquad (3.6)$$

local Reynolds stress:

$$\frac{\delta(uv)}{uv} = \sqrt{\left(\frac{\delta u}{u}\right)^2 + \left(\frac{\delta v}{v}\right)^2} = \sqrt{\left(\frac{\delta U_x}{u}\right)^2 + \left(\frac{\delta U_y}{v}\right)^2} \qquad (3.7)$$

$$= \delta U_x * \sqrt{\left(\frac{1}{u}\right)^2 + \left(\frac{1}{v}\right)^2} = \frac{\sqrt{(\delta s')^2 + (\delta s'')^2}}{\Delta t} * \sqrt{\left(\frac{1}{u}\right)^2 + \left(\frac{1}{v}\right)^2}$$

local turbulent intensity:

$$\frac{\delta\left(u^2/U_c^2\right)}{u^2/U_c^2} = \frac{\delta\left(u^2\right)}{u^2} = 2 * \frac{\delta u}{u} = 2 * \frac{\delta U_x}{u} = \frac{\sqrt{(\delta s')^2 + (\delta s'')^2}}{\Delta t} * \frac{2}{u} \qquad (3.8)$$

The uncertainty in the measured local vorticity is approximated by introducing the average, vorticity generating, velocity $\overline{U}_{side}$ along the sidelines of a gridbox. This velocity can be calculated by the average of the differences of the values of the two

velocities along opposide grid sidelines divided by 2(see also chapter 3.1.2). Because this velocity is the average of four independent velocities, its error and the error in the mesh size m is estimated by:

$$\delta \overline{U}_{side} = \frac{\sqrt{4 * \left(\frac{1}{4} * \sqrt{(\delta s')^2 + (\delta s'')^2} \right)^2}}{\Delta t}$$

$$= \frac{1}{2} * \frac{\sqrt{(\delta s')^2 + (\delta s'')^2}}{\Delta t} = \frac{1}{2 * \sqrt{2}} * \frac{\delta m}{\Delta t}$$

(3.9)

Assuming a square gridbox of the area A=m², the relative error in the vorticity is estimated to (see also equation 3.4):

local vorticity:

$$\frac{\delta \omega_z}{\omega_z} = \frac{\delta \left(\frac{1}{A} \int_C \vec{U} \bullet d\vec{S} \right)}{\left(\frac{1}{A} \int_C \vec{U} \bullet d\vec{S} \right)} \approx \frac{\delta \left(\frac{4 * \overline{U}_{side} * m}{A} \right)}{\left(\frac{4 * \overline{U}_{side} * m}{A} \right)} = \frac{\delta \left(\frac{\overline{U}_{side} * m}{m^2} \right)}{\left(\frac{\overline{U}_{side} * m}{m^2} \right)}$$

(3.10)

$$= \sqrt{\left(\frac{\delta \overline{U}_{side}}{\overline{U}_{side}} \right)^2 + \left(\frac{\delta m}{m} \right)^2} = \sqrt{\left(\frac{\delta m}{2 * \sqrt{2} * \Delta t * \overline{U}_{side}} \right)^2 + \left(\frac{\delta m}{m} \right)^2}$$

$$= \sqrt{(\delta s')^2 + (\delta s'')^2} * \sqrt{\left(\frac{1}{2 * \Delta t * \overline{U}_{side}} \right)^2 + \frac{F\sqrt{2} I^2}{Hm K}}$$

The error analysis shows that the fluid dynamic quantities that can be calculated from the location of the single intersection points, involve different uncertainties. Whereas the uncertainty of the local velocities is only a function of the accuracy in finding the intersection points of the undistorted and distorted grid and of the time delay Δt, the uncertainty of Reynolds stress and turbulent intensity is also a function of the expected local fluctuation in the velocity.

The uncertainty in the local vorticity is approximated by a function of the mesh size, a average velocity along the sidelines of the grid box, the reading error and the time delay Δt. A classical error analysis that indicates the expected error resulting from double differencing a grid to obtain vorticity is presented in reference [14]. To compare the performed relative error estimation of equation 3.10 to the classical analysis, equal assumptions are made. During a time interval Δt one sideline of a square grid of the meshsize m is displaced by m/2 in sideline direction. This leads to $\overline{U}_{side}=m/(8*\Delta t)$ and $\omega_z=1/(2*\Delta t)$ in equation 3.10.

Denoting the reading error $\sqrt{(\delta s')^2+(\delta s'')^2}$ as δs and replacing in equation 3.10 yields to:

$$\delta\omega_z = \frac{3}{\sqrt{2}}*\left(\frac{1}{\Delta t}\right)*\left(\frac{\delta s}{m}\right) \tag{3.10a}$$

The result of the analysis in reference [14] is:

$$\delta\omega_z = \left(\frac{1}{\Delta t}\right)*\left(\frac{\delta s}{m}\right) \tag{3.10b}$$

A higher constant is obtained with the present error analysis, however, both equations contain the same function of Δt, δs and m.

Since cameras of all kind are basically limited in their resolution (instrumental limitation), a minimum uncertainty of the measurement is always involved. The maximum accuracy intersection points can be determined is half of the resolution. The here employed camera detector provides a maximum resolution of 384 x 576 pixel which resolves the corner velocities of a 10% deformed, imaginable 384 x 384 pixel mesh, by 2% maximum.

Improve in the measurement accuracy of the velocity and hence in the other fluid mechanic properties can generally be achieved by increasing the time delay Δt, if the

resolution is unchanged. However, this requires larger mesh sizes and involves less local and temporal resolution of the fluid dynamic quantities. Increase in the resolution of the detector may decrease the minimum uncertainty but is only expedient if the actual reading accuracy of the intersection points is expected to be more precise than the current detector resolution permits.

The reliability of the value that is the average of fluid dynamic quantities calculated from single measurements is certainly larger, if mainly random errors occur (here: determination of intersection points by hand). Denoting the maximum occurring error in the reading of the intersection points by $\delta s'_{max}$ and $\delta s''_{max}$, the standard deviation is estimated by $\delta s'_s = 2/3 * \delta s'_{max}$ and $\delta s''_s = 2/3 * \delta s''_{max}$ [13]. If n is the number of measurements (distorted grids), then the (relative) standard error (R)SE of the fluid dynamic quantities is:

standard error of local velocity:

$$SE(\overline{U}_x) = \delta \overline{U}_x = \frac{1}{\sqrt{n-1}} * \frac{\sqrt{(\delta s'_s)^2 + (\delta s''_s)^2}}{\Delta t}$$

$$= \frac{2}{3 * \sqrt{n-1}} * \frac{\sqrt{(\delta s'_{max})^2 + (\delta s''_{max})^2}}{\Delta t}$$

(3.11)

relative standard error of local Reynolds stress:

$$RSE(\overline{uv}) = \frac{\delta(\overline{uv})}{\overline{uv}} = \delta \overline{U}_x * \sqrt{\left(\frac{1}{u'}\right)^2 + \left(\frac{1}{v'}\right)^2}$$

$$= \frac{2}{3 * \sqrt{n-1}} * \frac{\sqrt{(\delta s'_{max})^2 + (\delta s''_{max})^2}}{\Delta t} * \sqrt{\left(\frac{1}{u'}\right)^2 + \left(\frac{1}{v'}\right)^2}$$

(3.12)

relative standard error of local turbulent intensity:

$$RSE\left(\frac{u'}{U_C}\right) = \frac{\delta\left(\sqrt{\overline{u^2}}/U_C\right)}{\sqrt{\overline{u^2}}/U_C} = \frac{1}{2}*2*\frac{\delta\overline{U}_x}{u'} = \frac{\delta\overline{U}_x}{u'} \tag{3.13}$$

$$= \frac{2}{3*\sqrt{n-1}}*\frac{\sqrt{(\delta s'_{max})^2+(\delta s''_{max})^2}}{\Delta t}*\frac{1}{u'}$$

relative standard error of local vorticity:

$$RSE(\overline{\omega}_z) = \frac{\delta\overline{\omega}_z}{\omega_z} \tag{3.14}$$

$$= \frac{2*\sqrt{(\delta s'_{max})^2+(\delta s''_{max})^2}}{3*\sqrt{n-1}}*\sqrt{\left(\frac{1}{2*\Delta t*\overline{U}_{side}}\right)^2+\left(\frac{\sqrt{2}}{m}\right)^2}$$

Because the expected local fluctuation of the velocities does not change with the local averaging of the data, the standard error in the mean of all the shown fluid dynamic quantities alters with the same function of the number of measurements. Note u' and v' instead of $\overline{u}$ and $\overline{v}$ in the error equations of the mean local Reynolds stress and turbulent intensity. The root mean square quantities have been introduced because the mean of the fluctuation part of the velocities is zero by definition.

The confidence region (a quantity for the mean reliability) of the mean value is a function of the standard error, of t (a factor that is dependent on the required statistical safety and the number of measurements; see [15,16] and appendix E for t-distribution) and of the number of measurements. The deviation between the mean and the real value decreases with the number of measurements and decreases the confidence region of the mean value. The relative confidence region (RCR; confidence region: CR) of the fluid dynamic quantities (FDQ) as a function of the relative standard error (RSE; standard error: SE):

$$(R)CR_{FDQ} = \frac{t}{\sqrt{n}}*(R)SE_{FDQ} \tag{3.15}$$

To achieve a statistical reliability of 95% that the real fluid dynamic quantity is in the confidence region of the mean of 24 measurements of a fluid dynamic quantity (t=2.08, like for the performed experiments), the (relative) confidence region is:

$$(R)CR_{FDQ} \approx 0.43 * (R)SE_{FDQ} \qquad (3.16)$$

Measuring over an area of large mean velocity gradients may involve large relative uncertainty as well as large relative confidence region gradients over the measuring area if a constant time delay Δt is used. Assuming a constant uncertainty of evaluating the grid intersection points and a constant relative velocity fluctuation in the hole area, the absolute velocity fluctuations are small in areas of low mean velocity. Therefore, the relative error and the relative confidence region of the calculated fluid dynamic quantities is, respectively, proportional to $1/\Delta s$, hence to the reciprocal of the local mean velocity.

3.2 Implementation of the LIPA-technique in a free jet

3.2.1 Tracer gas, carrier gas and stimulation process selection

Because the turbulent length scales are small, a gaseous tracer is required for the implementation of the LIPA-technique in a free jet to follow the flow properly.

3.2.1.1 Tracer gas requirements

The selection of a adequate luminescent gas is critical. Fundamental requirements that must be met are:

- The luminescent lifetime must be long enough to trace the marked particles. Because a grid distortion of not more than 10% of the initial grid mesh size is requested, the required luminescent lifetime is a function of the expected velocities in the flow area of interest and of the initial grid mesh size. In order to obtain sufficient information for a jet formed by a 1 cm nozzle exit diameter, the maximum mesh size is set to about 5 mm. The jet core velocity to work with, is 17 m/s. Thus a luminescent lifetime of at least 60 μs (twice the lifetime to detect the grid after 10% distortion) is required.

- The luminescent emission must be of sufficient magnitude to permit detection of the 'distorted grid'. Luminescent intensity at a certain time after excitation, is a function of the quantum efficiency, the number of emitting molecules and the luminescent intensity decay over time. The latter, an important point for the tracer selection, has to be neglected because for most chemicals this function is not available. However, typically luminescence intensity decays exponentially over time. Thus, the relative luminescent intensity (normalized with the initial luminescent intensity) of a longer time emitting chemicals is expected to be higher compared to a shorter time emitting chemicals. If the laser intensity is high enough, the number of molecules emitting can be raised by seeding the flow with more luminescent molecules up to a limit that is given by the vapor pressure of the substance (at flow temperature). Thus a high

vapor pressure (commonly given at room temperature) of the luminescent substance is desired.

Further criteria for the tracer selection which, although not critical, can ease experimental implementation:

- to permit experiment implementation in air, luminescent emission should not be quenched by nitrogen, oxygen or other air components.

- to ease illumination and detection problems, the absorption and emission wavelength should be close or in the visible region.

- low cost

- no toxicity

The foregoing requirements are difficult to meet simultaneously. One drawback common to nearly all luminescent processes with long emission lifetime of chemicals in the gas phase, is the high quenching rate by oxygen. Also, substances with high vapor pressure tend to emit in the ultra violet, while those emitting in the visible tend to have vapor pressures considerably below 133.32 Pa (1 Torr). The most promising process is found in the phosphorescent emission of 2,3 butanedione ($CH_3COCOCH_3$) also known as biacetyl.

Because biacetyls phosphorescence is strongly quenched by oxygen, nitrogen is chosen as the carrier gas (see quenching rate constants in chapter 3.2.1.2.2).

The existing light source, a excimer laser which can emit light of 248, 308 and 351 nm with different gas fillings, can excite biacetyl at the border of its phosphorescing first allowed absorption region (350-465 nm). This may reduce the achievable quantum yield and lifetime of biacetyls phosphorescence. If the direct excited phosphorescence of biacetyl can not be detected, biacetyls phosphorescence can also be sensitized efficiently by triplet sulfur dioxide, generated by excitation of sulfur dioxide within a band of 240-

320 nm. The sulfur dioxide sensitized phosphorescence of biacetyl by excitation of a nitrogen-biacetyl-sulfur dioxide mixture with a wavelength of 308nm is expected to have a higher quantum yield and lifetime than the direct excitation of biacetyl in a nitrogen-biacetyl mixture.

3.2.1.2. Biacetyl

Biacetyl (2,3 butanedione, $CH_3COCOCH_3$ or Ac_2), a watery and yellowish liquid with a strong, distinctive odor, is used as a flavor in the diary industry. It is nontoxic (average U.S. adult's daily consumption is about 10 mg), freezes at about -3 °C and boils at 89 °C. Its vapor is flammable with a flash point of 70 °C. Biacetyl is one of the few substances whose luminescence behavior is quite similar in all three phases, solid, liquid and vapor. Therefore, among other reasons, it has been extensively studied over the past fifty years.

Biacetyl has at least three major advantages for use as a seed material for gases in laser marking:

- It has a relatively high vapor pressure of 5.3 kPa (40 Torr) at 20°C and shows no obvious condensation below 2.66 kPa (20 Torr) at 20°C, so that a gas flow can be easily seeded with it

- Its phosphorescence quantum yield Φ_p (defined as emitted intensity/absorbed intensity) can be as high as 15 % [7,17,18,19]

- Its phosphorescence lifetime can be reasonably long (practically up to 1.77 ms) [7,19]

Furthermore, the relatively low triplet energy of biacetyl (E_T=57 kcal/mol) allows efficient triplet energy transfer from a variety of molecules of photochromical interest (like SO_2).

The major shortcoming of biacetyl is the severe affection of its phosphorescence quantum yield and lifetime by oxygen quenching (see figure 12).
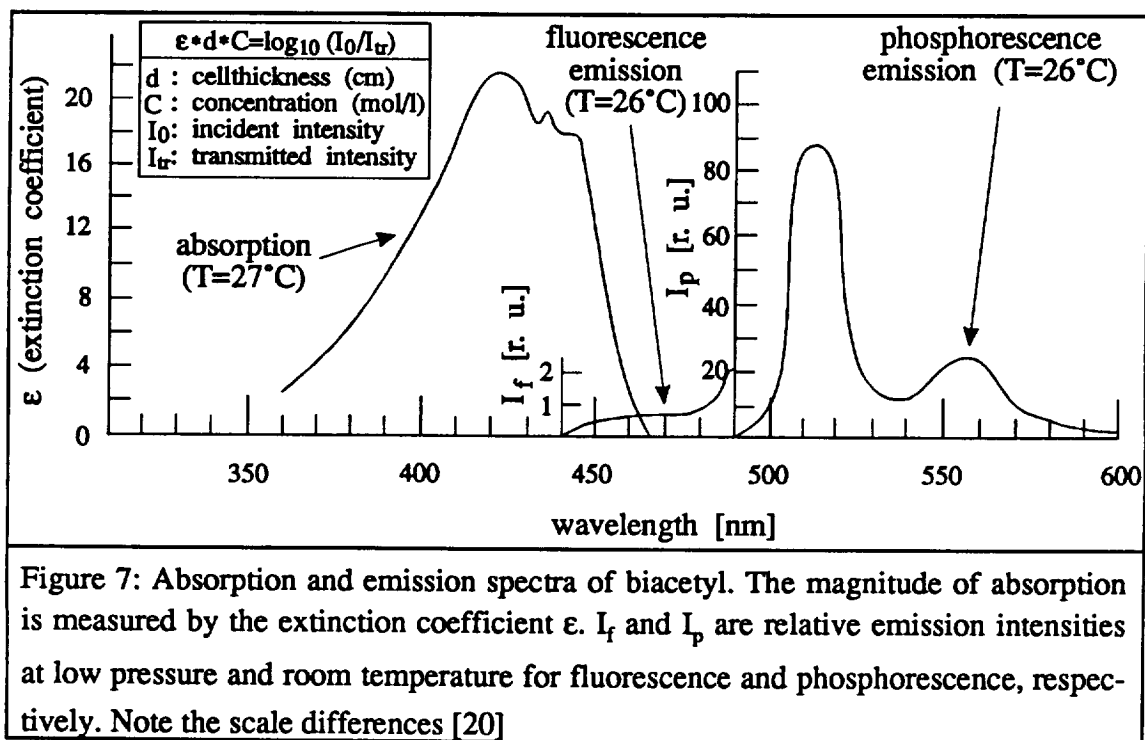
3.2.1.2.1 Photochemistry of biacetyl vapor and biacetyl vapor containing mixtures in a static cell

The photochemistry of biacetyl vapor is one of the most thoroughly studied and best understood of all the carbonyl compounds. This favorable situation exists largely as a result of the many definitive studies by Noyes and his colleagues [20,21,22,23,24]. More recently, the direct excited as well as the sulfur dioxide sensitized phosphorescence of biacetyl vapor and biacetyl vapor containing mixtures has been studied by Horowitz, Calvert, Sidebottom, Kommandeur, Moss and coworkers basically in cell experiments [17,18,25,26,27,28,29,30,31,32,33,34].

It shall be mentioned, that Horowitz and Calvert 1972 [17,26] found, that the observed effect of biacetyl pressure on the phosphorescent quantum yield in their cell experiments [26,35] resulted from biacetyl triplet decay at the cell wall, and concluded, that at least a major share of the earlier in cell experiments observed effect has the same origin.

3.2.1.2.2 Photochemistry of pure biacetyl vapor in a static cell

Biacetyl vapor displays a first allowed absorption band (350 - 465 nm) with a peak near 420 nm and a second allowed absorption band (220 - 320 nm) with a peak near 275 nm. Whereas the direct excitation of biacetyl within its second allowed absorption region produces no detectable emission [18], excitation of biacetyl within its first allowed absorption band creates fluorescent emission, a singlet-singlet transition which occurs between states of the same multiplicity (i. e., states of the same electronic spin) and phosphorescent emission, a triplet-singlet transition which occurs between states of different multiplicity.

Figure 7: Absorption and emission spectra of biacetyl. The magnitude of absorption is measured by the extinction coefficient ε. I_f and I_p are relative emission intensities at low pressure and room temperature for fluorescence and phosphorescence, respectively. Note the scale differences [20]

Fluorescence displays a emission range from 440 to 600 nm [20]. The fluorescent quantum yield of 0.25 % is essentially constant over a wide range of pressures (13.23 - 5333 Pa), temperatures (25 - 119 °C) and exciting wavelengths (385 - 450 nm) [7,20,21,29]. The lifetime of the fluorescent emission is reported to be 10^{-8} to 10^{-6} s at 25 °C for excitation from 365 to 435 nm and pressures from 40 to 5333 Pa [5,18,23,30]. Unfortunately no temperature dependent lifetime studies have been reported for the fluorescence of biacetyl vapor. The fluorescent emission of biacetyl vapor is not quenched by oxygen [30].

Biacetyls phosphorescent emission region extents from 490 nm to 600 nm with a peak near 510 nm. At room temperature, pumping near the absorption peak of about 420 nm and biacetyl pressures from 13 to 5332 Pa, biacetyl phosphorescence displays a lifetime of 1.54 ± 0.23 ms. Its quantum yield of about 15 ± 3 % is essentially constant over a range of exciting wavelengths (365 - 440 nm) and pressures (1.5 - 533.32 Pa) [18,20,21,22]. At low wavelengths (< 380 nm) pressure must be high enough to prevent dissociation (> 267 Pa).

Unlike the fluorescence, the phosphorescence quantum yield and lifetime of biacetyl vapor is strongly dependent on temperature [17,18,19,23,27]. The phosphorescence emission intensity as well as the lifetime decrease considerably with rising temperature above 50 °C.

Figure 8 and 9: Logarithmic decay of biacetyl phosphorescence intensity and temperature dependence of biacetyl phosphorescence lifetime for 435 nm excitation. Data from Jian-Bang and coworkers [19] covers: total pressure 0.1 - 0.8 bar; biacetyl pressure 46 - 5507 Pa; $[Ac_2]/[N_2]$ 0.001-0.30
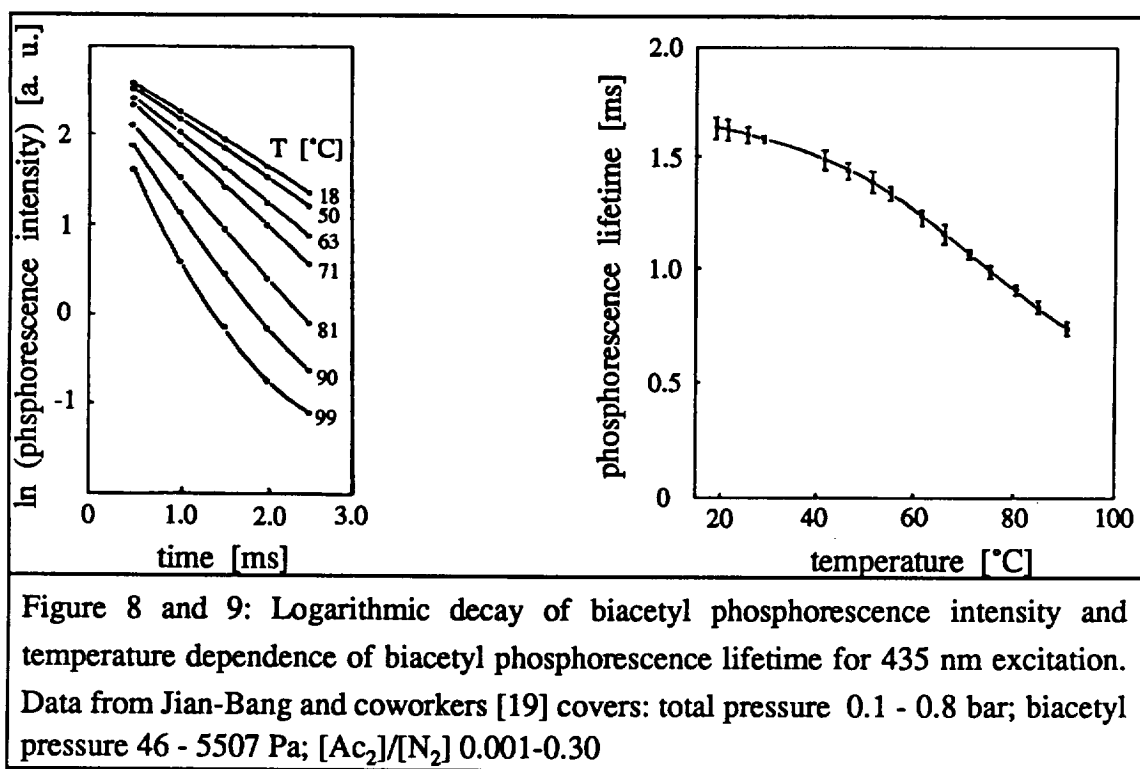
As a means of understanding the biacetyl luminescence process, it is useful to examine the excitation scheme (figure 10).

The luminescent processes are as followed. Molecules can be pumped by absorption of energy from the ground singlet state S_0 (^1A_g) to the singlet state S (^1A_u; zeroth level ca. 64 kcal/mol above the ground state [29]). Most of the molecules in the S state radiationlessly transit to the triplet T (^3A_u; zeroth level ca. 57 kcal/mol above the ground state [23,26]) (quantum yield $\cong$ 1 [7,22,29]) under the perturbation of the spin-orbit coupling (S $\rightarrow$ T intersystem crossing, an intramolecular process and independent of pressure [7,22,29]), the other return to the S_0 state via either the S $\rightarrow S_0$ internal conversion or the spontaneous transition emitting fluorescence. Some of the molecules in the T state

```
ISC : INTERSYSTEM CROSSING
IC  : INTERNAL CONVERSATION
VR  : VIBRATIONAL RELAXATION
D   : DISSOCIATION
S_0 : GROUND STATE
S   : SINGLET
T   : TRIPLET
```

VR   ISC   D $2(CH_3CO)$
IC   ISC
S   ISC   VR
VR   T
$h\nu$ ABSORPTION $h\nu$ FLUORESCENCE $h\nu$ PHOSHORESCENCE
S_0

Figure 10: Biacetyl excitation scheme. [7,36]
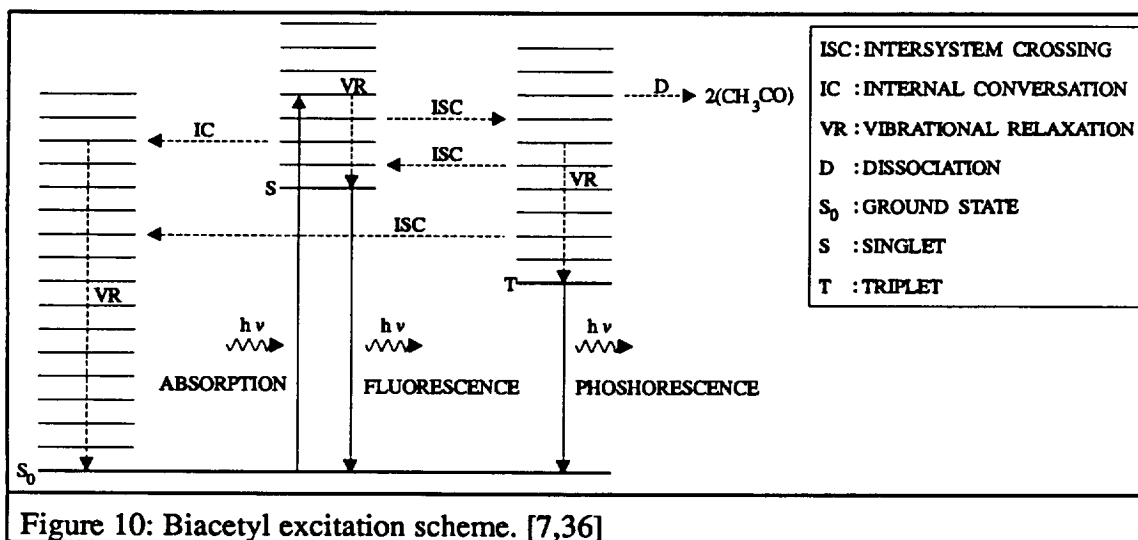
return to the ground state S_0 via $T \rightarrow S_0$ intersystem crossing or the phosphorescence transition (quantum mechanically forbidden with a long radiative lifetime of 10 ms) with a actual observed lifetime of 1.54 ± 0.23 ms at 25°C [18,29]. The other either transit to S via the $T \rightarrow S$ intersystem crossing or dissociate into $2(CH_3CO)$ (about 70 kcal/mol for the ground state molecule necessary to dissociate [26,29]). It is also possible that the biacetyl molecules in the T state are quenched by colliding with molecules of other species, but except a few species including the O_2, the quenching rate constant is quite small [17,18,19,29].

The actually observed lifetime of the phosphorescence transition is shorter than the radiative lifetime due to two important processes:

- A annihilation reaction between two molecules in the triplet state (quenching rate constant: $k=4.2 \pm 1.7 \times 10^{14}$ cm³/(mole*s) [31]). The significance of this path increases with concentration of triplet molecules and, hence, also with laser power. It should be emphasized, however, that although the time constant is shorter at higher laser intensities, the absolute phosphorescence yield is still enhanced, if the laser intensity used does not reach the saturation value of triplet biacetyl formation. Thus, high laser intensities might be desirable [7,18].

- Collisional de-excitation (quenching) also shortens the observed phosphorescence lifetime. Self-quenching, quenching by sulfur dioxide and quenching by nitrogen are far less important than quenching by oxygen (quenching rate constants in cm^3/(mole∗s): $k_{self} \cong 4 \times 10^6$ [18]; $k_{SO_2} \cong 4 \times 10^6$ [18]; $k_{N_2} \cong 10^6$ [7]; $k_{O_2} \cong 5 \times 10^{11}$ [17,18]). The latter is a strong quencher essentially precluding use of biacetyl in systems containing air. On the other hand, the low nitrogen quenching rate allows operation over a wide range of nitrogen background pressure, a fact that was verified in a static cell at total pressures between 1.3 kPa (10 Torr) and 100 kPa (1 atm). [7,36]

3.2.1.2.3 The SO$_2$-sensitized phosphorescence of biacetyl vapor in a static cell

Sulfur Dioxide has three main regions of absorption in the near ultraviolet: A first very weak forbidden absorption band from 340 - 390 nm, a stronger, first allowed absorption region from 240 - 320 nm and a still stronger absorption in the 190 - 220 nm region [28,37,38,39].

Static cell experiments by Horowitz, Calvert and coworkers [24,25,26,34] have demonstrated that the excited triplet state of sulfur dioxide ($^3SO_2$) is the primary reactive entity formed in the photolysis of sulfur dioxide irradiated within the second allowed absorption band (240 - 320 nm). The main route by which triplet sulfur dioxide molecules are formed is a second-order intersystem crossing reaction involving the singlet sulfur dioxide molecule ($^1SO_2$) and some collision partner.

Within the first allowed absorption band of SO$_2$ (240 - 320 nm) irradiated mixtures of sulfur dioxide and biacetyl demonstrated, that the incoming light was only absorbed by SO$_2$, and that the phosphorescence in biacetyl can be sensitized by triplet sulfur dioxide molecules.

Even small amounts of biacetyl added to within its first absorption band irradiated sulfur dioxide show a decrease in the phosphorescence of sulfur dioxide (380 - 470 nm) and a sensitized quantum yield of biacetyl emission (Φ_{sens}). Rao and coworkers [27] showed, that relative small biacetyl pressures (5 Pa) quenched the phosphorescence (lifetime $\cong$ 0.4 ms [28,37]) of sulfur dioxide (84 - 293 Pa) completely and did not lower detectably the emitted fluorescence (lifetime $\cong$ 0.02ms [27]) of sulfur dioxide. Note in figure 11, that in the mixture the phosphorescence of SO_2 is quenched considerably and the sensitized phos-
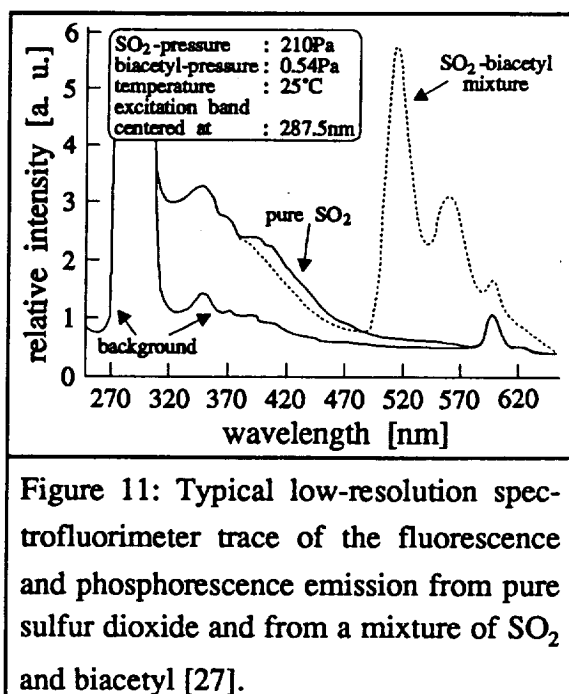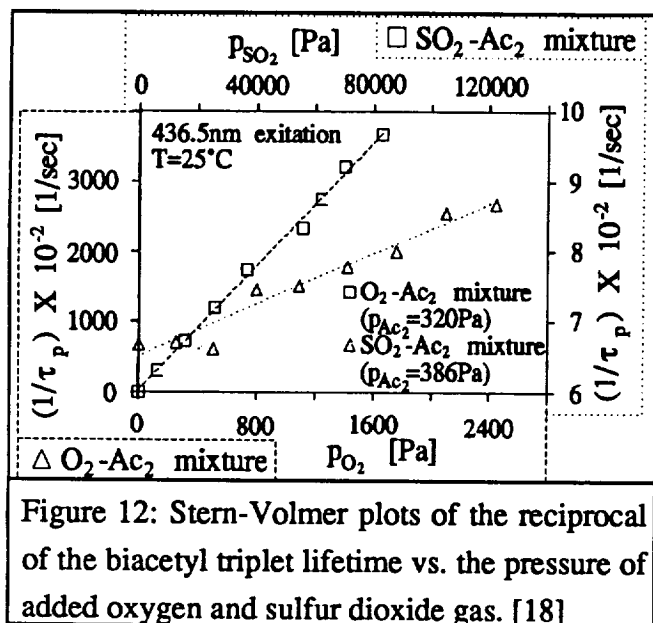

Figure 11: Typical low-resolution spectrofluorimeter trace of the fluorescence and phosphorescence emission from pure sulfur dioxide and from a mixture of SO_2 and biacetyl [27].

phorescence emission of biacetyl appears (quenching rate constant for $^3SO_2$ quenching by biacetyl: 1.42 X 10^{-11} l/(mol*s)).

For [SO_2] / [Ac_2] concentrations from 60 to 600 and SO_2 - pressures of 85 - 550 Pa, Horrowitz and Calvert [25] found in static cell experiments, that the reciprocal of the quantum yield of the sensitized phosphorescence in biacetyl is, respectively, a linear function of the reciprocal of the total pressure (for [SO_2] / [Ac_2] = const.) and of the concentration ratio (for SO_2 - pressure = const.).

Whereas the Φ_{sens} dependence on the [SO_2]/[Ac_2] ratio is anticipated theoretically, the Φ_{sens} dependence on the total pressure for fixed concentration ratios is theoretically unexpected and is probably largely the result of biacetyl triplet diffusion with deactivation at the cell wall (diffusional effects at the cellwall decrease with pressure) [17,26]. Unfortunately new data from experiments in larger cells has not been reported.

Figure 12: Stern-Volmer plots of the reciprocal of the biacetyl triplet lifetime vs. the pressure of added oxygen and sulfur dioxide gas. [18]

The lifetime of triplet biacetyl phosphorescence in biacetyl-SO_2 and biacetyl-oxygen mixtures has been investigated by Sidebottom and coworkers [18], by exciting the mixtures within the second allowed absorption band of biacetyl. They showed, that the lifetime of biacetyl triplet in biacetyl-SO_2 mixtures is relatively insensitive to change in added SO_2 pressure for biacetyl pressures of 1.6 Pa and 386 Pa, whereas biacetyl triplet is quenched very effectively even at small oxygen pressure.

No lifetime measurements of biacetyl phosphorescence in within the first allowed absorption band of sulfur dioxide excited biacetyl-SO_2 mixtures have been published.

3.2.1.2.4 The 'excess' SO_2-sensitized biacetyl phosphorescence at high added gas pressures in a static cell

In static cell experiments Horrowitz and coworkers [25,38] determined the quantum yields of sensitized biacetyl phosphorescence emission for SO_2-biacetyl-N_2 mixtures irradiated within the first absorption band of SO_2. Experiments at constant concentration ratios ([N_2] : [Ac_2] : [SO_2] = 255 : 1 : 1) with N_2 pressures from 0.08 bar to 0.7 bar at 25°C were performed.

The data, that can not be explained by the investigated mechanisms at low pressure (<0.013bar) [26,35], reveals the Φ_{sens} continues to rise as the total pressure of the gas mixture is increased ('excess' biacetyl phosphorescence). Since there is no

significant increase in quantum yield of phosphorescence on increasing the pressure of added N_2 gas from 0.01 to 1 bar in biacetyl-nitrogen mixture, a SO_2 species seems to be responsible for the 'excess' biacetyl phosphorescence.

The results reported in Horrowitz and coworkers work [25,38] offer support for the existence of a undefined species X. In irradiated SO_2 systems at high pressure it is suggested, that X is not a triplet species which can transfer energy directly to biacetyl, but may form $^3SO_2$ rather efficiently on collision with added gases.

Figure 13: Plot of the reciprocal of the quantum yield vs. the reciprocal of the total pressure for data from a N_2-Ac_2-SO_2 mixture photolysis [25]

Unfortunately no lifetime studies have been reported for the 'excess' sulfur dioxide sensitized phosphorescence of biacetyl at high added gas pressures. Since the direct excited phosphorescence lifetime of biacetyl is, respectively, not influenced by high added N_2 pressure and added SO_2 pressure, the lifetime of the SO_2-sensitized phosphorescence of biacetyl is be expected to be independent on added N_2 or SO_2 (above a minimum SO_2 pressure) pressure.
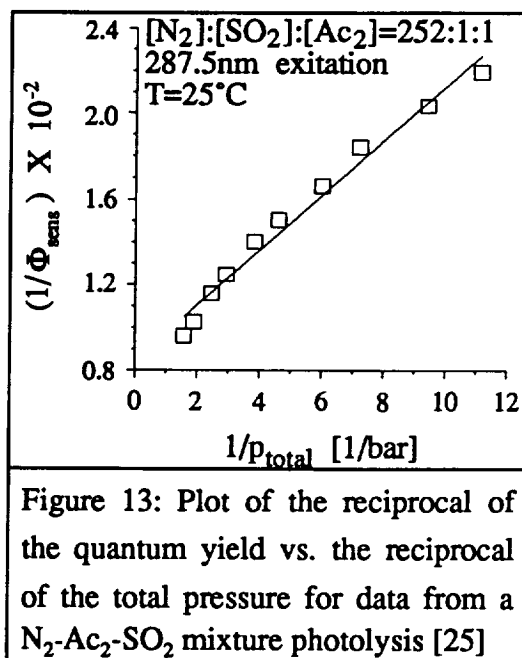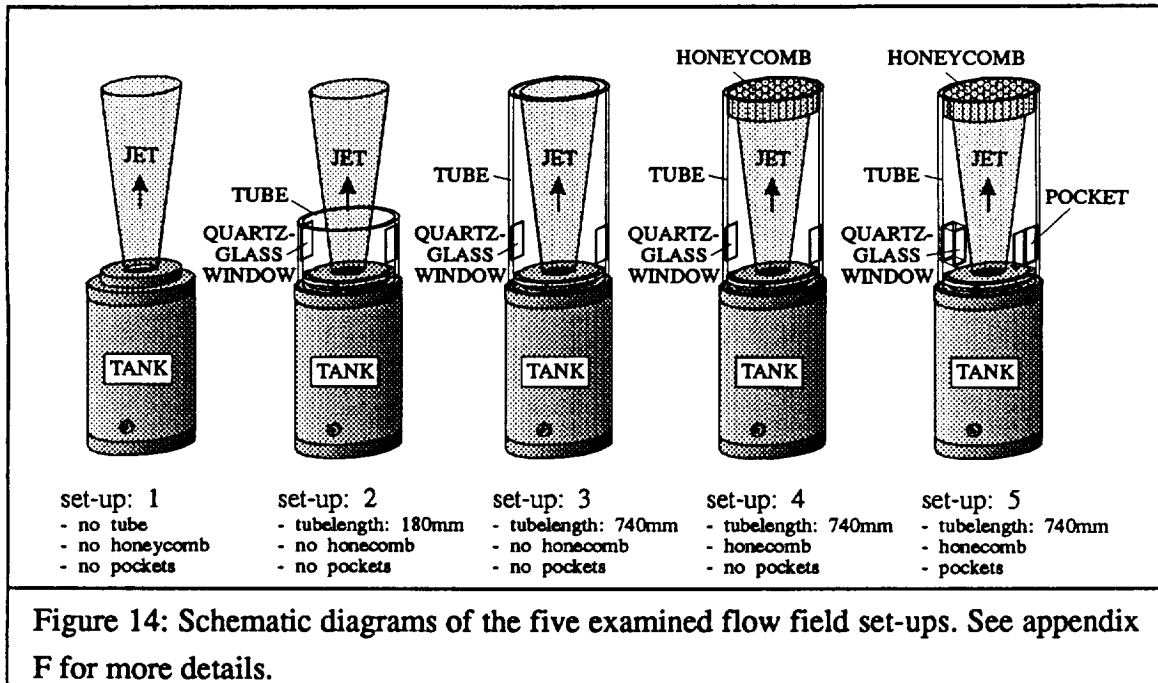
3.3 Performed experiments

LIPA experiments and the lifetime experiments are performed with nitrogen-biacetyl gas mixtures ($[N_2]:[Ac_2]=200:3$) and the set-up that is shown in figure4. The experiments with a still camera, that replaces the ICCD-camera assembly in figure 4, are performed with varying concentration ratios of nitrogen-biacetyl-sulfur dioxide gas mixtures and different flow generating set-ups (see figure 14). The core jet velocity for all experiments is, respectively, 17 m/s. A co-axial annular jet is provided if the main jet is issued into a tube. Relating to a preliminary experimental set-up and space, the annual jet is supplied further away from the initial jet as desired. The gas mixture component concentration in the side jet is, respectively, the same as in the main jet.

The concentration ratio for biacetyl in the gas mixture is measured by the decrease of liquid biacetyl in the mixing chamber during a certain time interval. The sulfur dioxide flow ratio is measured by a flowmeter in the sulfur dioxide support line.

3.3.1 Still camera experiments

In order to optimize the detectable biacetyl emission, experiments using a still 35mm camera instead of the ICCD camera (see figure 4) are performed. A uniform grid pattern brightness over a wide area in- and outside the potential jet core is desired. The camera is equipped with a 58mm (f-stop: 1:1.2) and a close-up lens and is loaded with 3200 ASA (Kodak T-MAX P3200) film material. The camera-shutter and the laser are operated manually. To capture all the emitted light, the camera-shutter is opened before the laser is fired and closed after the emission disappears. Pictures of the whole grid, as well as pictures of only one line (blocking of the other grid-lines, hence same energy in this one line as in one line of the hole grid) are taken. To keep the experimental set-up simple, we tried to find a set-up that allows the experiment to be performed in an open system, although biacetyls phosphorescent emission is strongly quenched by oxygen. Five different set-ups that are shown in figure 14 were examined.

Figure 14: Schematic diagrams of the five examined flow field set-ups. See appendix F for more details.

Using a Pitot-tube, the main jet velocity is measured to be ,respectively, 17 m/s in the potential core. Hence, performing experiments with one grid-line, considering the expected flow-field and the lifetime (1.8 ms) of the sensitized biacetyl emission, pictures taken of the emission are sumilar to that shown in figure 15. Whereas the excited particles in the central core of the jet are supposed to move with decreasing emission intensity (see chapter 3.2.1.2.2) over a distance, that is given by the detectable lifetime of the emission and by the jet velocity, the distance excited molecules in the mixing area are expected to move decreases with the distance from the central core because the mean velocity decreases.

Nitrogen gas as well as nitrogen-sulfur dioxide, nitrogen-biacetyl and nitrogen-bi-acetyl-sulfur dioxide gas mixtures of the initial jet (same gas mixture in side jet) have been examined to determine the performance of the sensitized biacetyl phosphorescence. Different sulfur dioxide concentrations at constant biacetyl concentrations in the initial jet have been examined in order to optimize the detectability of the emission.

The different flow generating set-ups (see figure 14) have been employed to reduce the oxygen concentration in the measuring area. Lower oxygen concentration, hence better detectability because of less quenching of the phosphorescent emission, is expected for issuing the jet into a tube (set-up: 2). A longer tube-length (set-up: 3) and a pressure gradient providing honeycomb in the tube outlet (set-up: 4) is expected to decrease oxygen concentration further. The pockets (set-up: 5; see appendix F) are added to decrease the energy loss along the incoming laser lines before reaching the measuring area (see chapter 4.1).
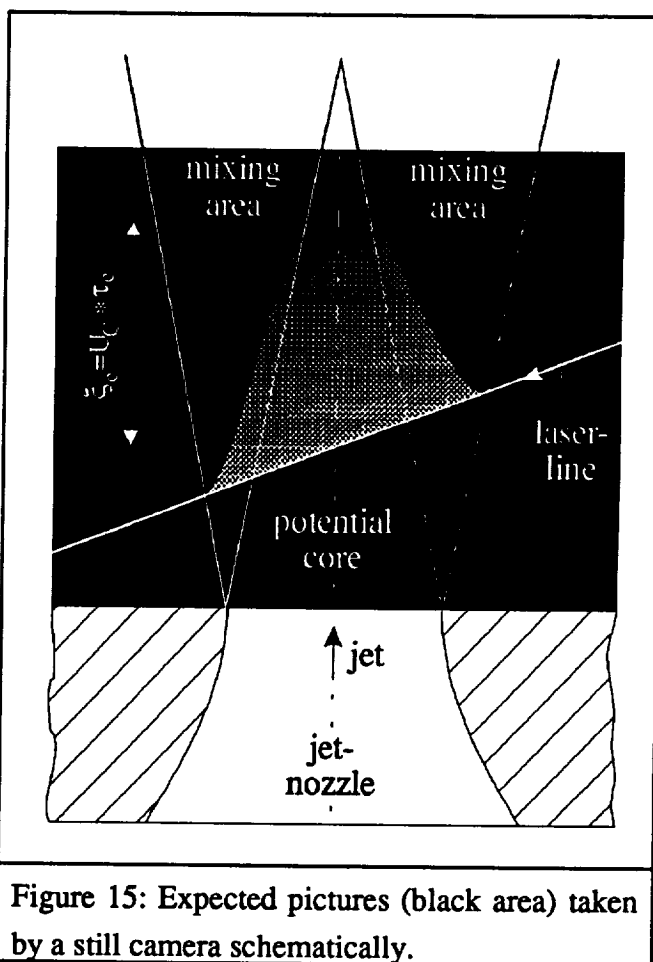
Figure 15: Expected pictures (black area) taken by a still camera schematically.

The taken pictures are presented in appendix B.

3.3.2 ICCD camera experiments

3.3.2.1 LIPA experiments

For the data sets presented here, an overall measurement area of approximately the distance from the jet centerline of ±3 y/r, and the distance from the jet nozzle in streamwise direction of 0 to 8.5 x/r was used. 18 incoming laserlines create 47 intersections and 30 grid boxes in the measuring area. The mesh size of the generated grid boxes spreads from about 4.2 to 5.2 mm.

Figure 16: Four raw LIPA data grids of a 17m/s nitrogen-biacetyl jet, taken with delay times of 0, 30, 60 and 90 µs after the laser pulse.
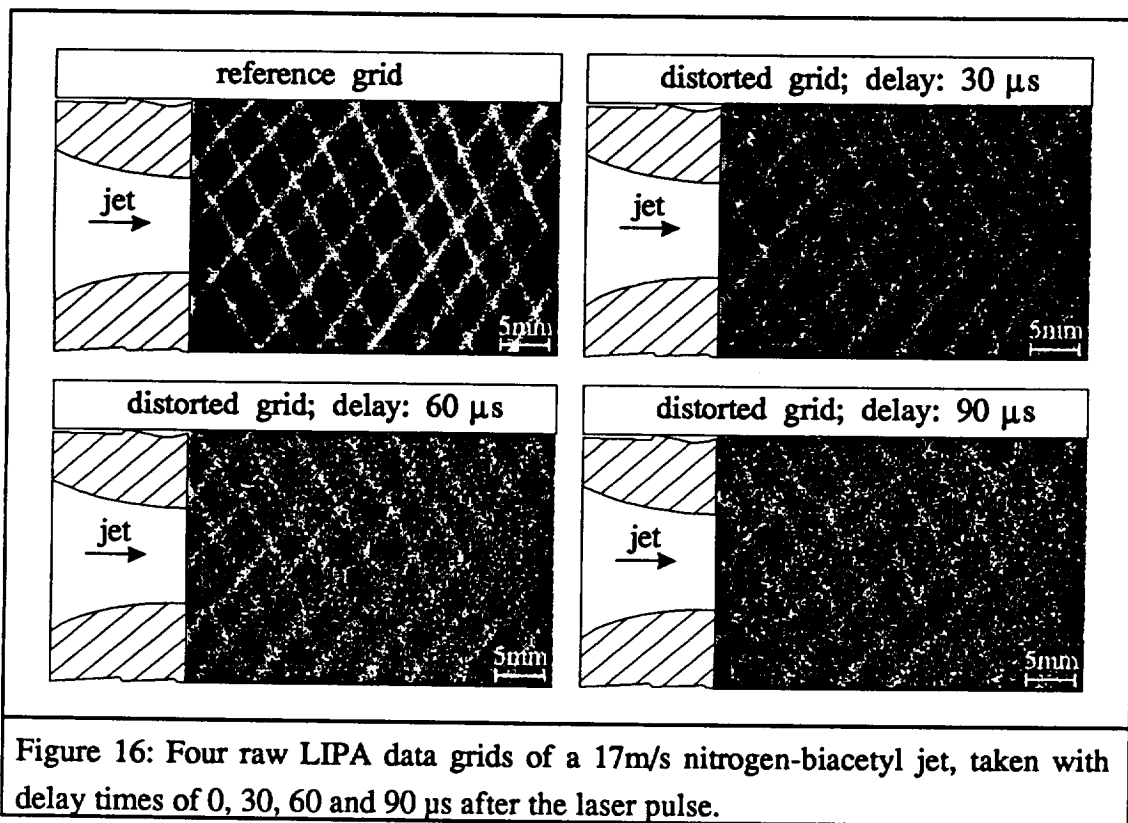
The chosen measuring area provides a data resolution of 0.0735 mm/pixel on the detector. The data frames are taken with a gating time of 0.095 µs, providing a maximum line movement during gating of a distance smaller than 1.7 µm, hence a maximum movement of 2.5% of the associated pixel distance on the detector. Whereas reference grids are taken when the laser fires, distorted grids are take at 30, 60 and 90 µs after the laser pulse (four raw data frames are shown in figure 16).

The excimer laser is set to provide 220mJ during a pulse length of 20ns with a repetition rate of 3 pulses per second (internal laser trigger). Each laser line carries approximately 6.6mJ. The grid plane is located above the centerline of the jet exit nozzle and has a thickness of the same order as the width of each beam (about 0.5mm).

Because the emission of a by 308nm excited nitrogen-biacetyl mixture of a molecular concentration $[N_2]:[Ac_2]=200:3$ (mass concentration of biacetyl ≈ 5%) can be easily detected with uniform brightness over the measurement area, the data grids are

taken without added sulfur dioxide gas. Experiments made with added sulfur dioxide gas show a ununiformity of emission over the measured area. The brightness of the lines in the potential core area of the jet increased more than in the surrounding area. Adjusting the camera intensification for the bright lines involve less contrast in the darker areas, hence less detectability in the darker area. To take maximum advantage of the dynamic detector range, a uniform line brightness in the hole picture area is required.

Pockets, as they are employed in the still camera experiments to decrease the energy loss along the laserline, are not employed in the LIPA experiments. The disturbance of the flowfield is considered to be not negligible, hence no pockets are used.

3.3.2.2 Lifetime experiments

In order to measure the detectable lifetime of the biacetyl emission in a set-up, that is the same as in the LIPA experiments, the ICCD camera is set to maximum intensification. The same gain duration as in the LIPA experiments (0.095µs) is employed. To generate a higher contrast in the picture area, the side-jet is not seeded with biacetyl. In order to gain a even higher signal-noise performance of the expected weak signals, 5 pixels along both axes are software binned.

Binning in software is chosen because the hardware binning uses shift registers and binning capacitors that are only approximately twice the size of regular pixels. In order not to loose the true signal value, hardware binning is therefore limited to 2 pixels. Implementing software binning, the CCD is read out using combined pixels sufficiently small to avoid saturating the shift registers or binning capacitors. These stripes are then added in the software producing a resultant combined pixel that represents more photons than is possible only using hardware binning.

The signal noise performance is generally improved by binning because the extra noise collected with each additional stripe read is negligible compared with improvement in the photon signal to noise ratio due to the overall large number of photons collected. Although binning reduces the image resolution, wherefore it is not been implemented for

the LIPA experiments, it is applied for the lifetime experiments where high intensification and signal to noise ration is more important than high resolution.

Examples of pictures taken are shown in appendix D. To prevent the CCD array from overexposure, pictures for time delays smaller than $\Delta t = 0.5$ms are not taken. Smaller delays are associated with brighter phosphorescence.

4. Results

4.1 Still camera experiments

Unlike experiments using nitrogen-biacetyl-sulfur dioxide mixtures ($[N_2]$:$[Ac_2]$:$[SO_2]$=200:3:2 to 200:3:5), pure nitrogen gas, nitrogen-sulfur dioxide ($[N_2]$:$[SO_2]$=200:1 to 200:5) and nitrogen-biacetyl ($[N_2]$:$[Ac_2]$=200:5) gas mixtures of the initial jet do not emit detectable emission, whichever flow generating set-up (see appendix B) is used. The maximum length of detectable emission in streamwise direction is approximately ξ_e=25mm. Considering a core velocity of 17m/s, a 'lifetime' of about 1.5ms can be detected with the applied equipment (see chapter 3.3.1). Because of the detected 'lifetime' and the absence of detectable emission in nitrogen, nitrogen-biacetyl and nitrogen-sulfur dioxide gas mixtures, the detected emission in experiments using nitrogen-biacetyl-sulfur dioxide gas mixtures is assumed to origin by sulfur dioxide sensitized phosphorescence of biacetyl.

Performed experiments with set-up: 1 show that the emission in the central core of the jet can be easily detected, whereas there is no detectable emission in and outside the mixing area of the jet even with high present sulfur dioxide concentrations (up to: $[SO_2]$=1.3 X $[Ac_2]$) in the initial jet. The detectable emission increases by rising the sulfur dioxide concentration from $[N_2]$:$[Ac_2]$:$[SO_2]$=200:3:1 to 200:3:5. Quenching of the biacetyl phosphorescence by oxygen is assumed causing this lack of detectable emission in- and outside the mixing area.

Issuing the jet into a short tube (set-up 2; tubelength: 180mm) increases the detectable emission in the central core region of the jet reasonably. The same tendency of emission intensity with increasing sulfur dioxide concentration as in set-up 1 can be observed. However, outside of the jet area no emission can be detected. Quenching of the biacetyl phosphorescence by oxygen because of the relative long distance between the side jet and the main jet is assumed to be responsible for this absence of detectable emission outside the jet.

By issuing the jet into a longer tube (set-up 3; tubelength: 740mm), the intensity of the detectable emission in the central core of the jet reduces to a level less than for set-up 2, however, emission outside the potential core can be easily detected. The absorption along the incoming laser line, outside the potential core, is made responsible for the reduced emission level in the central jet area. Because in set-up 3 emission even outside the jet can be detected, the absorption along the laser line in- and outside the shown area may be reasonably higher than in set-up 2, hence less energy in the incoming laser line and less detectable emission.

A maximum of emission intensity between $[N_2]:[Ac_2]:[SO_2]$ ratios of 200:3:1 and 200:3:3 is detected for experiments with set-up 3. The picture area in appendix B shows about 30% of the total laser line inside the tube. Assuming homogeneous gas concentrations along the incoming laser line and no saturation effects, the decay of the laser intensity I_l along the laser line [41] coordinate x_l may be approximated by $I_l \approx I_{l_0} * \exp(-\alpha x_l)$. Assuming the absorption coefficient to be linearly dependent on the sulfur dioxide concentration in the illuminated gas volume $\alpha \approx C_2 * [SO_2]$ and a linear dependence of the emitted light intensity on the sulfur dioxide concentration and the illuminating light intensity $I_e \approx C_1 * I_l * [SO_2]$, the emitted light intensity I_e may be roughly approximated by the relation $I_e \approx C_1 * I_{l_0} * [SO_2] * \exp(-C_2 * [SO_2] * x_l)$. This relation shows the existence of a maximum emission intensity at a constant position on the laser line as a function of sulfur dioxide concentration in the gas mixture. However, a maximum emission intensity may not occur in the experiments if the optimum sulfur dioxide concentration for a x-coordinate in the picture area is not exceeded. Experiments with set-up 1 and 2 do not show a existence of a maximum emission intensity because the origin of the coordinate x_l is at the edge of the jet, hence lower x_l-values. Nevertheless this may explain the existence of a maximum emission intensity as it is observed in experiments with set-up 3.

A further decrease of detectable emission of excited nitrogen-biacetyl-sulfur dioxide mixtures occurs by plugging the tube outlet of set-up 3 with a honeycomb. An overall decrease of detectable emission in comparison to set-up 3 is observed. As well as in the experiments using set-up 3, a maximum of the emission intensity can be detected

within the applied concentration ratios in set-up 4. The same explanation as in the foregoing paragraph shall be given.

In set-up 5 'pockets'(see appendix F) are implemented to rise the laser line energy in the picture area, by reducing the length on which absorption of the laser line energy can occur before entering the picture area by about 50%. Obviously the detectable emission intensity is much higher than in experiments with set-up 4, which supports the above given explanations.

4.2 LIPA experiments

From initially 40 recorded data frames, 24 data frames of distorted grids with 47 intersection points each are reduced on the image processor. The data frames of the distorted grids are taken 60μs after the reference grid which is, respectively, taken at the time of the laser pulse. The gaiting time for the camera intensifier is adjusted to 0.095μs. The fluid dynamic properties which are the mean velocity components, the Reynolds stress, the turbulent intensity and the vorticity are calculated. In appendix C the results are shown in form of tables, vectorplots and contourplots.

Because the data reduction on the image processor is performed by hand (finding the grid intersection points with a software cross on a 1024x1024 pixel screen) a random error in locating the intersection points occurs. This uncertainty in location the proper intersection points is assumed to generate the major error in the experimental data and is therefore particularly examined (see also chapter 3.1.3). In order to evaluate the reading error and hence the experimental error, several readings of different intersection points in a variety of different data frames are performed. The maximum deviation from the average location of the readings is determined to 3 pixel of the initial data resolution for the distorted grids and to 1 pixel of he initial data resolution for the reference grid.

The difference in the position of the distorted and undistorted intersection points occurs because of the fluid motion during luminescent emission decay with time and because of diffusion. Typically phosphorescent emission decays exponential with time

(see chapter 3.2.1.2.2). Applying the same dynamic range (14-bit detector, but just 8-bit for data reduction) for different maximum light emission intensities at unchanged background light intensity will reduce the contrast, the background noise or both. Because a small contrast as well as a high background noise render reading more difficult, hence, less reproducible and accurate. The broadening of the visible lines, which happens as a result of diffusion (mainly turbulent diffusion) that on average carries emitting fluid volume out of the excited fluid volume does not necessarily influence the reading accuracy of the intersection points (the reading of the center point is still accurate as long as the border of the area can be well determined), but the associated decrease of contrast reduces accuracy.

The measured mean velocity distribution is shown in appendix C. Velocities of the order of the expected core velocity are measured at measuring points in the area around the jet axis (ly/rl<1.2). Slow, negative streamwise velocity is determined for measuring points in the interval 2.2<ly/rl<2.9, whereas slow streamwise velocity is determined for the other measuring points. The measured y-component of the mean velocity is only larger than 1m/s at some measuring points at ly/rl>2.2.

Considering a circular jet of uniform velocity coming out of a nozzle into a large stagnant mass of the same fluid, the generated flow field is commonly sectioned into a potential core, an annual shear layer and the ambient fluid. Due to the velocity discontinuity at the plane of the nozzle, shear stresses are set up and a shear layer originates. In most of the practical cases, this shear layer becomes turbulent very close to the nozzle itself. On the inside it invades into the uniform velocity jet and penetrates into the ambient fluid on the outer side.

In order to compare the measured velocity field to other experimental results in the literature, the measuring area is divided into the three common areas by the empirical equations [42]:

$$\left|\frac{y_1}{r}\right| = 0.95 - 0.097 * \frac{x}{r} \qquad (4.1)$$

$$\left|\frac{y_2}{r}\right| = 1.07 + 0.158 * \frac{x}{r} \qquad (4.2)$$

with: y_1 - inner edge of mixing region

y_2 - outer edge of mixing region

Whereas the core velocity (inside the inner edge of the mixing region) is expected to be constant and equal to U_C, the velocity outside the mixing region is expected to be equal to zero. Inside the mixing region, the velocity distribution is predicted with the cosine function of Squire and Trouncer [42]:

$$\frac{U_x}{U_C} = \frac{1}{2} * \left[1 - \cos\left(\pi * \frac{y_2 - y}{y_2 - y_1}\right)\right] \qquad \text{for:} \left|\frac{y_1}{r}\right| < \left|\frac{y}{r}\right| < \left|\frac{y_2}{r}\right| \qquad (4.3)$$
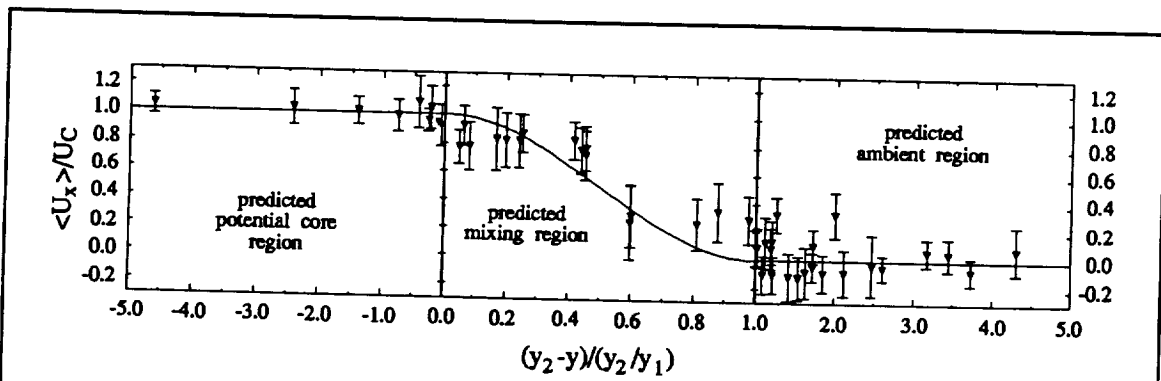
Figure 17: Comparison of the measured velocity to the empirical equation of Squire and Trouncer [42]. ▼: here performed measurements with rms-errors; ——: Squire and Trouncer (equation 4.1 to 4.3).

Denoting the average of the streamwise velocities in the estimated central core as the core velocity U_C leads to the distribution in figure 17 and to the deviations $(U_{x_{estimate}} - U_x)$ shown in table C1. Inside the central core region velocity deviations up to 1.28m/s can be observed, whereas maximum velocity deviations of 4.79m/s and 5.23m/s occur in the mixing and ambient region.

Agreement with the predicted velocity distribution in the potential core region and in the inner half of the mixing region is better than in the area further away from the jet-axis. The observed deviations from the empirical velocity distribution as well as the measured negative streamwise velocities in the ambient region imply a significant influence of the surrounding tube and the secondary flow on the velocity field. Particularly the measured negative streamwise velocities hint to a recirculation zone typically observed for jet mixing in a duct [10].

The general result of high velocity jet mixing in a duct is increasing static pressure along the flow direction. The produced pressure gradient can effect a massive rearrangement of the flow. Selecting a variable area duct to keep the static pressure constant can prevent recirculation. Here, however, an axial pressure gradient is required to obtain a low oxygen concentration in the measuring area. Special conditions have been determined in the literature where the flow remains 'similar' even in the presence of an axial pressure gradient [10,43,44].

The velocity, turbulence intensity and Reynolds stress data obtained have been compared to measurements by Hussain and Clark [45], Crow and Champagne [46] and Sami, Carmody and Rouse [47]. The Mach numbers of the free jets in the reference-experiments is sufficiently low that the flow can be considered incompressible. The Reynolds numbers of these experiments are higher than in the present measurements (Re_d= 360000, 106000 and 220000 compared to 12000), but lower Reynolds number data for the developing region of a free jet has not been found in the literature. In order to compare the measured fluid dynamic quantities to the literature-data, the measuring area is sectioned into 7 intervals in flow direction. Plots of the quantities in this 7 intervals are shown in appendix C (figure C11).

A peak of the Reynolds stress and turbulent intensity distribution at |y/r|≅1 as well as a minimum at |y/r|=0 is predicted [9,10,42,45,46,47]. Neither of these predictions can be observed in the actual data. Compared to the calculated Reynolds stress, the calculated turbulent intensity is rather equally distributed over the measuring area. Both do not show a significant tendency or symmetry.

As well as the Reynolds stress and the turbulent intensity, the mean vorticity distribution is expected to have a maximum at $|y/r| \cong 1$ and a minimum at $|y/r| = 0$. The latter can be easily observed in figure C9 and C10. For the 6 measuring points close to the jet symmetry-axis the measured vorticity expands from -241 to 340 1/s. The vorticity seems to increase with the distance from the jet axis to a maximum between $1 < |y/r| < 2$. The calculated vorticity-data shows qualitative as well as quantitative symmetry to the jet axis.

4.3 Lifetime experiments

Because the slow co-axial jet that formed an annulus jet has not been seeded with biacetyl, only the potential core and the mixing region of the 1cm central jet can be seen as the bright area in the pictures shown in appendix D.

The jet area can be easily observed with decreasing light intensity up to a delay time of 2.5ms. For longer time delays the jet contour disappears slowly and the light-intensities of the background and the jet become similar. For the implemented flow conditions and detection equipment, a reasonable limit of time delays applicable for LIPA is found to be 2.0 to 2.5 ms.

The illumination of the jet is performed with the same laser grid pattern as in the LIPA experiment. The impressed grid pattern can not be observed. Two factors can be thought of being responsible for the disappearance of the grid pattern:

- The resolution of the pictures made here is lower than in the LIPA-experiments. 5x5 pixels of the resolution implemented in the LIPA experiment are binned (see chapter 3.3.2.2). With this resolution a initial grid-box has a sidelength of approximately 15 binned pixel blocks. This may cause likely smoothing of the image, but can not be made individually responsible for the lack of grid pattern.

- Diffusion causes exchange of emitting and non emitting molecules between the excited and not excited flow volumes. By the exchange of the molecules the

impressed lines widen. Because the diffusion is a function of time, the width of the emitting lines increases with the time delay Δt. The diffusion length l_d of the excited molecules during the delay time $\Delta t = 60\mu s$ can be calculated with the solution for the boundary layer of the suddenly accelerated plane wall ([48], page 83):

$$l_d = \sqrt{v * \Delta t} \approx 0.03 \text{ mm} \tag{4.4}$$

Compared with the full image resolution of 0.0735 mm/pixel (with binning only 0.3675 mm/pixelblock) the diffusion should be negligible as well as the maximum line-movement of 0.0016 mm during the 95 ns gating time. The magnitude of the calculated diffusion length does not support considerable influence of the diffusion on the disappearance of the grid pattern.

5. Discussion

If illumination, hence grid generation, shall be performed with a wavelength of 308nm, the use of sulfur dioxide to sensitize biacetyls phosphorescence might be desirable for the implementation of the LIPA-technique in a gas flow. As in the static cell experiments reported in the literature and in the presently employed experimental conditions, the sulfur dioxide-concentration in a 308nm irradiated sulfur dioxide-nitrogen-biacetyl mixture can effect the emitted light intensity significantly.

For the present investigation, the stimulation process and concentration ratios of the mixture components, the presence of sulfur dioxide increased irradiated light intensity considerably. However sulfur dioxide can increase the efficiency of the stimulation, the use of the sensitizer sulfur dioxide for the LIPA-technique requires adjustments that may not always be matched. The observed decrease of emission intensity along a laserline even for small sulfur dioxide concentrations, makes a adjustment of mainly two parameters necessary. The length, laser beams pass through the test atmosphere, and the sulfur dioxide concentration in the gas mixture have to be adapted.

In principle, absorption along the laser line always takes place if excitation occurs. Direct excitation of biacetyl closer to its absorption peak by a dye-laser may cause a similar effect as remarked. Higher absorption and hence higher decrease of energy may cause observable decrease of emission intensity along a incoming laser beam as a function of biacetyl pressure. Because implementation of the LIPA-technique desires homogeneous emission intensity of the laser lines in the measuring area, the different experimental parameters are to be optimized. In general a high quantum yield, hence a high conversion rate of absorbed to emitted intensity, is desired in order to generate bright and homogeneous grid-lines.

The present performed LIPA-experiments are performed with a nitrogen-biacetyl gas mixture. Sulfur dioxide is not employed because inhomogeneous emission intensities in the measuring area are observed by adding the sensitizer of biacetyls phosphorescence to the gas mixture. Besides the described absorption along the grid-lines, mainly

inhomogeneous gas mixture over the measuring area is made responsible for this effect. Considering, respectively, the similar molecular weights of biacetyl and sulfur dioxide, the concentration distribution of this two gases is assumed to be similar over the measuring area. The concentration of these two gases is expected to be the highest in the central core, where the oxygen concentration is supposed to be the lowest. Support for this assumption is provided by the high emission intensities in the central core that could have been observed within the still camera experiments. Taking the limited dynamic range of the detector and the high differences of emission intensities over the measuring area in account, can explain the inhomogeneity of the detected emission intensity. A sulfur dioxide concentration that provides reasonable signal-noise improvement without generating the mentioned disadvantages has not been not found for the employed set-up. By the results of the still camera experiments it is expected to be in the range of $[SO_2]<[N_2]/200$ for $[N2]:[Ac2]=200:3$. However, a sulfur dioxide-concentration ratio in this range can not be properly adjusted in the here employed set-up.

The presented error analysis (chapter 3.1.3) permits evaluating the accuracy of the calculated fluid dynamic properties. The error analysis predicts a tendency of decreasing accuracy in the obtained velocity, vorticity, turbulent intensity and Reynolds stress data which is supported by the experimental results. The plots in appendix C show a qualitative as well as quantitative high rate of symmetry for the velocity and vorticity field. In contrast no general tendency of the turbulence intensity and Reynolds stress data could be observed. Furthermore, a random Reynolds stress distribution with a peak that is not explainable is observed.

In order to reevaluate the accuracy of the obtained data, the reading error is approximated by the observed velocity deflection in the central core ($\Delta U_x=1.28$m/s; see chapter 4.2). Neglecting errors of other origin than reading errors $\delta s'$ and $\delta s''$, hence calculating reading errors by the obtained velocity deviation in the predicted central core, leads to a à posteriori evaluation of the obtained data. This appraisal guides to a deterioration of the à priori estimation of the data precision by a factor of about 5 ($\Delta U_x=1.28$m/s à priori compared to the à posteriori calculated confidence region of 0.25m/s).

A comprehensive explanation for this discrepancy can not be given. One important factor may be the duct effect on the flow field. Unsymmetrical, oscillating recirculation zones have been observed in a duct under some flow conditions by Curtet [10]. If a similar flow-field has been generated in this work, the observed velocity defection in the potential core may be generated by a oscillating potential core.

Some suggestions for future improvement of the performance of the LIPA-technique in general, and measurements in a jet in particular shall be made here:

- To resolve the velocity more uniformly over the whole measuring area, different time delays for areas of different velocity have to be implemented. If supported by the sampling rate of the equipment, this can be achieved by taking pictures of distorted grids at different time delays during one illumination process. If the equipment does not provide a fast enough sampling rate the areas of different velocity should be measured at separate excitation processes. The time delay Δt should be adapted to the velocities in the flow regions.

- In order to improve local resolution, smaller mesh sizes or a larger orifice diameter might be desirable. The creation of smaller grid sizes in the order of 1mm or even smaller, may require implementation of a different beam dividing technique. Easing of handling and adjusting as well as more distinguished grid-lines should be the main goals. The use of diffraction gratings or fiber optics may be worth to be further examined. A larger orifice diameter might be required to resolve the expected peaks in the fluctuation and vorticity distribution as they are shown in appendix C.

- Improvements in the flow generation have to be achieved. Since oxygen has to be kept out of the measuring area, an open air system will always require a pressure gradient. According to literature free jet characteristics as well as a pressure gradient can be accomplished in a duct. If the relative simple set-up of a open system shall be retained, changes on the duct have to be made to realize free jet characteristics.

- Implementation of a closed system for the flow generation. Issuing the jet into, or generating the jet inside a large, with nitrogen and biacetyl vapor filled, box can provide free jet characteristics. Generating the flow-field of interest inside a closed box would make a more precise adjustment of the gas mixing ratios as well as a more homogeneous mixing possible. Generating of the flow-field could be established by replacing the bottom plate of the tank used in the present experiments by a fan, that forces the flow through the nozzle. Placing this set-up into a closed loop-system filled with the desired gas mixture is a suggestion that would also allow forestalling quenching of biacetyls phosphorescence by oxygen without the need of a duct.

- A more homogeneous gas mixture of nitrogen and biacetyl may be desirable. Realizing seeding with a carburetor or a fuel injection like functioning system can improve homogeneity as well as provide more accurate concentration ratio data.

- If a better evaluation of the grid-intersections is attained, a higher resolution of the image capturing device can improve accuracy of the technique. Film material in combination with image intensification or higher resolved CCD arrays may be helpful. Considering automatization of the technique, a digital data acquisition rather than a analog technique should be preferred.

- Achieving more accuracy in the calculated fluid dynamic quantities requires evaluation of a much larger number of frames than it is done in this work. Therefore automated data reduction is necessary. Computer programs that are currently being worked on may offer this in the near future.

6. Conclusions

- The experiments are conducted in an completely gaseous environment with properties very near to those of air.

- A jet in a recirculating co-axial flowing environment is studied.

- Recirculation outside the generated jet can be observed. Re-entrainment of the central jet is likely. In order to provide complete free jet characteristic the set-up has to be changed. Changes on the duct according to literature or the use of a closed system are suggested.

- On average, the velocity vector field picture for the predicted jet area of the central core and the mixing region looks like expected. High velocities in the central core and decreasing velocities in the mixing zone are measured.

- The tendency of the mean vorticity distribution perpendicular to the jet axis looks like expected. Small vorticity close to the jet axis, increasing positive vorticity in positive y-direction and increasing negative vorticity in the negative y-direction. Unfortunately only one vorticity measuring point is far enough away from the jet axis to show the increase of vorticity for high y/r (>2).

- The accuracy of the performed data reduction does not provide reasonable results for Reynolds stress and turbulence intensity distribution in the measuring area.

- The error analysis presented can be used to predict the accuracy in the calculated mean of the fluid dynamic quantities velocity, vorticity, turbulent intensity and Reynolds stress if the reading errors are known.

- Even using the present simple experimental set-up, and direct excitation of biacetyls phosphorescence at the border of its absorption band (308nm), we can generate detectable emission with a observed lifetime of about 3ms.

- Implementing phosphorescence of biacetyl vapor for the LIPA-technique requires a low oxygen concentration in the measuring area even if sensitizing of the emission by sulfur dioxide is used. A lower oxygen concentration than in the present experiments may improve the detectability of grid patterns.

- The use of sulfur dioxide to sensitize biacetyls phosphorescence is desirable if 308nm excitation of the gas mixture is employed. The observed high absorption of incoming laser light by gaseous sulfur dioxide in the mixture requires more sophisticated concentration adjustment techniques.

Appendix A: List of references

[1]   Falco, R. E.; Chu, C. C.; Hetherington, M. H.; Gendrich, C. P.; 1988; The
       Circulation of an Airfoil Starting Vortex Obtained from Instantaneous Vorticity
       Measurements Over an Area; American Institute of Aeronautics and Astronautics-
       88-3620-CP; 1048-1054.

[2]   Falco, R. E.; Chu, C. C.; 1987; Measurement of Two-Dimensional Fluid
       Dynamic Quantities Using a Photochromic Grid Tracing Technique. Society of
       Photo-Optical Instrumentation Engineers, # 814, Photomechanics and Speckle
       Metrology, 706-710.

[3]   Lambda Highlights; 1989; A Publication by Lambda Physik; #15/16.

[4]   Hilbert, H. S.; Falco, R. E.; 1991; Measurements of Flows During Scavening in a
       Two-Stroke Engine; SAE Technical Paper, 910671.

[5]   Epstein, A. H.; 1977; Qualitative Density Visualization in a Transonic
       Compressor Rotor. Journal of Engineering for Power, July (1977), 460-475.

[6]   McKenzie, R. L.; Monson, D. J.; Exberger, R. J.; 1979; Time-Dependent Local
       Density Measurements in Unsteady Flows. NASA Technical Memorandum
       78555, N79-18297.

[7]   Hiller, B.; Booman, R. A.; Hassa, C.; Hanson, R. K.; 1984; Velocity
       Visualisation in Gas Flows using Laser-Induced Phosphorescence of Biacetyl.
       Rev. Sci. Instrum. 55 (12), 1964-1967.

[8]   Abramovich, G. N.; 1963; The Theory of Turbulent Jets (USSR), MIT Press.

[9]   Pai, S. I.; 1954; Fluid Dynamics of Jets, Van Nostrand, New York.

[10]   Schetz, J. A.; 1980; Injection and Mixing in Turbulent Flow, Progress in
       Astronautics and Aeronautics. American Institute of Aeronautics and
       Astronautics, New York, New York.

[11]   Nelson, G. O.; 1972; Controlled Test Atmospheres; Ann Arbor Science
       Publishers.

[12]   Taylor, J. R.; 1982; An Introduction to Error Analysis; University Science Books,
       Oxford University Press.

[13]   Pentz, M; Shott, M.;1988; Handling Experimental Data; Open University Press
       Milton Keynes, Philadelphia.

[14]   Falco, R. E.; Gendrich, C. P.; Chu, C. C.; 1989; Vorticity Field Measurments Using Laser Induced Photchemical Anemometry (LIPA). Seventh Symposium on Turbulent Shear Flows, Stanford University.

[15]   Kuchling, H.; 1989; Taschenbuch der Physik; Verlag Harri Deutsch, Germany.

[16]   Bartsch; 1984; Taschenbuch mathematischer Formeln; Verlag Harri Deutsch, Germany.

[17]   Horowitz, A.; Calvert, J. G.; 1972; Emission Studies of the Mechanism of Gaseous Biacetyl Photolysis at 3450, 3650, 3880, and 4358 Å and 28° C. International Journal of Chemical Kinetics, Vol. 4, 207-227.

[18]   Sidebottom, H. W.; Badcock, C. C.; Calvert, J. G.; Rabe, B. R.; Damon, E. K.; 1971; Lifetime Studies of the Biacetyl Excited Singlet and Triplet States in the Gas Phase at 25°. J. Amer. Chem. Soc., Vol. 12 (1972), 13-19.

[19]   Jian-Bang, L.; Qi, P.; Chang-Sheng, L..; Jie-Rong, S.; 1988; Principles of Flow Field Diagnostics by Laser Induced Biacetyl Phosphorescence. Experiments in Fluids, # 6, 505-513.

[20]   Okabe, H.; Noyes, W. A.; 1956; The Relative Intensities of Fluorescence and Phosphorescence in Biacetyl Vapor. J. Amer. Chem. Soc., Vol. 79 (1957), 801-806.

[21]   Coward, N. A.; Noyes, W. A.; 1954; The Fluorescence in Biacetyl Vapor at 4358A. J. Chem. Phys., Vol. 22 (1954), 1207-1210.

[22]   Ishikawa, H.; Noyes, W. A.; 1962; Triplet State of Benzene. J. Amer. Chem. Soc.; Vol. 84 (1962), 1502-1503.

[23]   Cundall R. B.; Davies, A. S.; 1967; Primary Processes in the Gas-Phase Photochemistry of Carbonyl Compounds. Progr. Reaction Kinet.; Vol. 4 (1967), 149-214.

[24]   Hiller, B.;McDanniel, J. C.; Rea, E. C.; Hanson, R. K.; 1983; Laser-Induced Fluorescence Technique for Velocity Filed Measurements in Subsonic Gas Flows. Optics Letters, Vol.: 8 (1983), 474-476.

[25]   Horowitz, A.; Calvert, J. G.; 1973; The Kinetics of Biacetyl Phosphorescence Sensitized in 2875 Å-Irradiated SO_2-Biacetyl-Added Gas (CO_2, CO, N_2) Mixtures. The Nature of the SO_2 Excited States Formed at High Added Gas Pressures. International Journal of Chemical Kinetics, Vol. 2, 243-260.

[26]   Horowitz, A.; Calvert, J. G.; 1972; The SO_2-Sensitized Phosphorescence of Biacetyl Vapor in Photolyses at 2650 and 2875 Å. The Intersystem Crossing Ratio in Sulfur Dioxide. International Journal of Chemical Kinetics, Vol. 4 ,175-189.

[27]   Rao, T. N.; Collier, S. S.; Calvert, J. G.; 1968; Primary Photophysical Processes in the Photochemistry of Sulfur Dioxide at 2875 Å. J. Amer. Chem. Soc., Vol. 91 (1969), 1609-1615.

[28]   Sidebottom, H. W.; Badcock, C. C.; Calvert, J. G.; Rabe, B. R.; Damon, E. K.; 1970; Mechanism of th Photolysis of Mixtures of Sulfur Dioxide with Olefin and Aromatic Hydrocarbons. J. Amer. Chem. Soc., Vol. 93 (1971), 3121-3129.

[29]   Conchenanainnn, C. O.; Sidebottom, H. W.; 1979; Temperature Dependence of the Triplet Lifetime of Biacetyl in the Gas Phase. Journal of Photochemistry, # 13 (1980), 55-66.

[30]   van der Werft, R.; Kommandeur, J.; 1976; The Electronic Relaxation of Biacetyl in the Vapor Phase. Chemical Physics, # 16, 125-150.

[31]   Badcock, C. C.; Sidebottom, H. W.; Calvert, J. G.; Rabe, B. R.; Damon, E. K.; 1971; A Study of the Triplet-Triplet Annihilation Reaction in Biacetyl Vapor Excited at 4365 A 25°. J. Amer. Chem. Soc.; Vol. 94 (1972), 19-24.

[32]   van der Werft, R.; Schutten, E.; Kommandeur, J.; 1976; The Electronic Relaxation of Methylgloxal in the Vapor Phase. Chemical Physics, Vol.: 16 (1976), 151-159.

[33]   van der Werft, R.; Schutten, E.; Kommandeur, J.; 1975; Slow, Fast and Dual Fluorescence in Glyoxal Vapor. Chemical Physics, Vol.: 11 (1975), 281-288.

[34]   Moss, A. Z.; Yardley, J. T.; 1974; Radiationless Decay from Triplet State Biacetyl Molecules with Selected Vibrational Energies. J. Chem. Phys., Vol.: 61 (1974), 2883-2889.

[35]   Horowitz, A.; Calvert, J. G.; 1972; A Study of the Intersystem Crossing Reaction Included in Gaseous Sulfur Dioxide Molecules by Collisions with Nitrogen and Cyclohexane at 27° C. International Journal of Chemical Kinetics, Vol. 4 ,191-205.

[36]   Paul, P. H.; van Cruyningen, I.; Hanson, R. K.; Kychakoff, G.; 1990; High Resolution Digital Flowfield Imaging of Jets. Experiments in Fluids, # 9, 241-251.

[37] Sidebottom, H. W.; Badcock, C. C.; Calvert,Reinhardt, G. W.; J. G.; Rabe, B. R.; Damon, E. K.; 1970; A Study of the Decay Processes in the Triplet Sulfur Dioxide Molecule Excited at 3828.8 Å. J. Amer. Chem. Soc., Vol. 93 (1971), 2589-2592.

[38] Wamper, F. B.; Horowitz, A.; Calvert, J. G.; 1971; Mechanism of Carbon Dioxide Formation in 3130 Å Irradiated Mixtures of Sulfur Dioxide and Carbon Monoxide. Journal of the American Chemical Society, Vol. 94, # 16, 5523-5536.

[39] Stricker, S. J.; Howell, D. B.; 1968; Luminescence and Radiations Transitions in Sulfur Dioxide Gas. J. Chem. Phys,; Vol 49 (1968), 1947-1951.

[40] Cehelnik, E.; Spicer C. W.; Heicklen, J.;1970; Photolysis of Sulfur Dioxide in the Presence of Foreign Gases Carbon Monoxide and Perfuoroethylene. J. Amer. Chem. Soc.; Vol. 93 (1971), 5371-5380.

[41] Sparrow, E. M.; Cess, R. D.; 1978; Radiation Heat Transfer. McGraw-Hill.

[42] Rajaratnam, N.; 1976; Turbulent Jets; Developments in Water Science, #5; Elsevier Scientific Publishing Company.

[43] Fekete, G. I.; 1964; Two-Dimensional Self-Preserving Turbulent Jets in Streaming Flow. McGill Univ., Rept. MERL 70-71, 1970.

[44] Oosthuizen, P. H.; Wu, M. C.; 1979; Experimental and Numerical Study of Constant Diameter Ducted Jet Mixing. Turbulent Shear Flows I, Springer-Verlag, Berlin, Germany.

[45] Hussain, A. K. M. F.; Clark, A. R.; 1979; On the Coherent Structure of the Axissymmetric Mixing Layer: a Flow-Visualisation Study. Journal Fluid Mechanics, (1981), Vol. 104, 263-294.

[46] Crow, S. C.; Champange F. H.; 1970; Orderly Structure in Jet Turbulence. Journal Fluid Mechanics, (1971), Vol. 48, 547-591.

[47] Sami, S.; Carmody, T.; Rouse, H.;1966; Jet Diffusion in the Region of Flow Establishment, Journal Fluid Mechanics, (1967), Vol. 27, 231-252.

[48] Schlichting, H.; 1968; Boundary-Layer Theory; McGraw-Hill Book Company, New York.

[49] List, E. J.; 1982; Turbulent Jets and Plumes; Annual Review of Fluid Mechanics, # 14, 189-212.

[50] Aldrich; 1990-1991; Catalog Handbook of Fine Chemicals.

[51] Karlekar, B. V.; 1983; Thermodynamics for Engineers; Prentice-Hall.
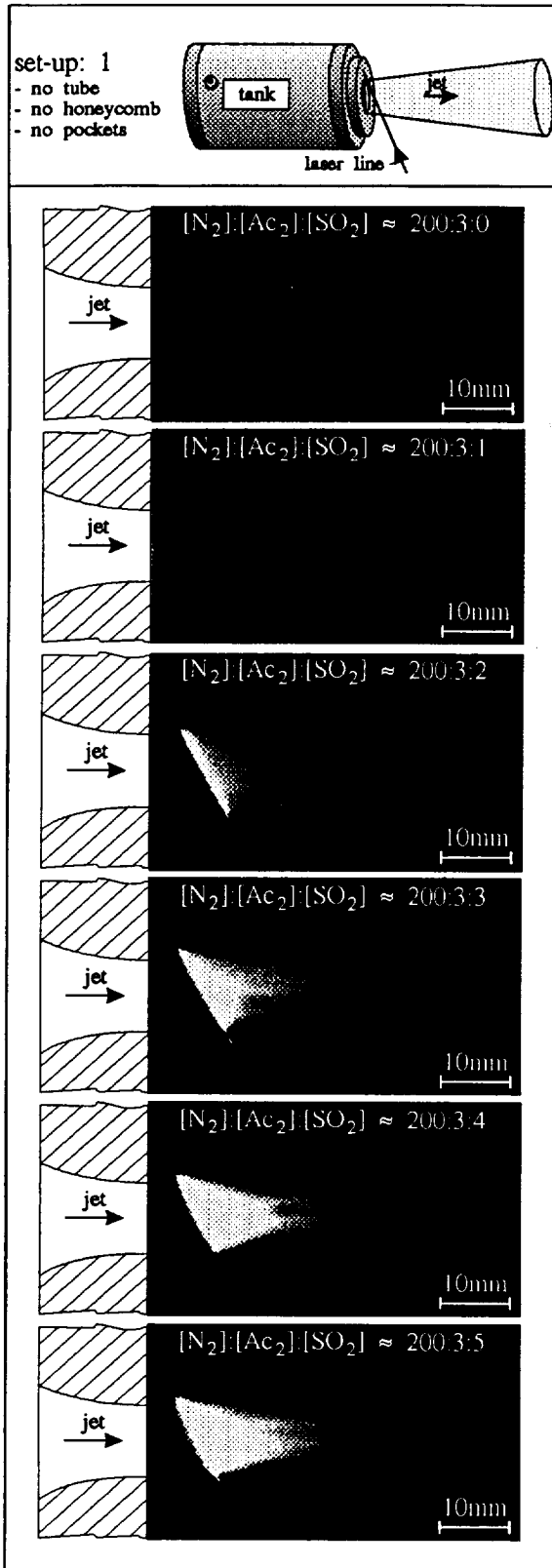
Appendix B: Data still camera experiments
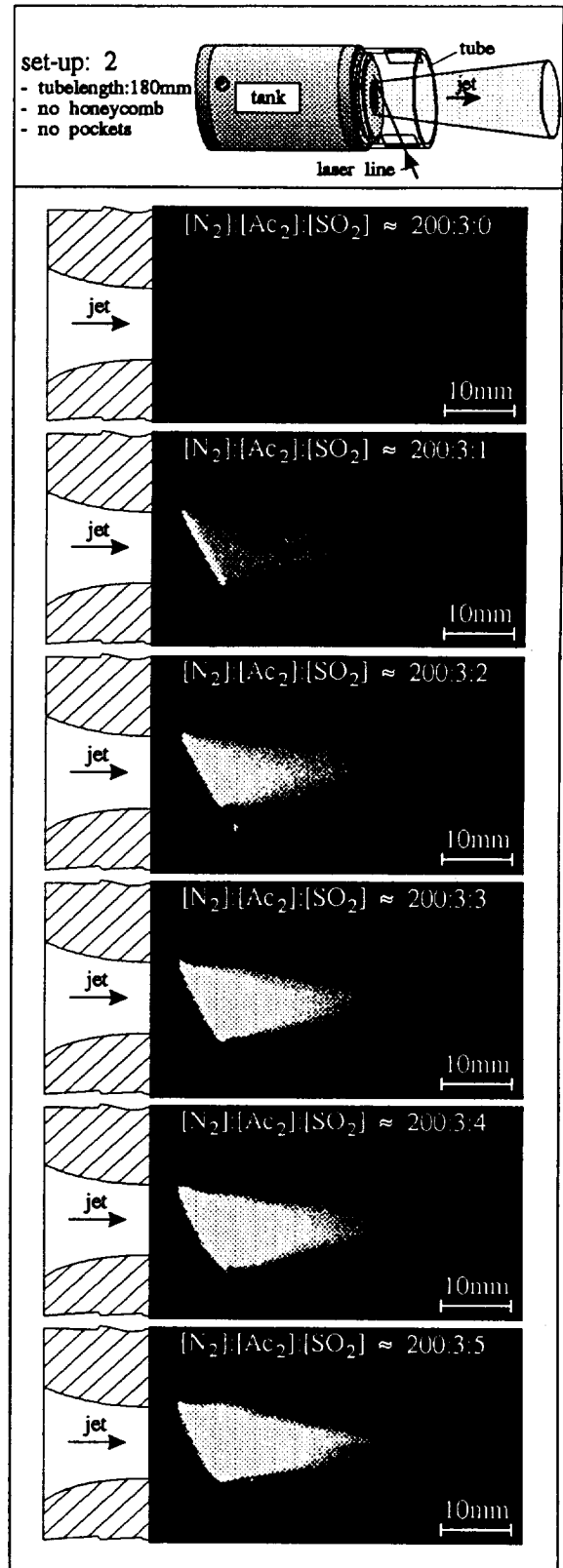

Figure B1: Taken pictures for set-up 1

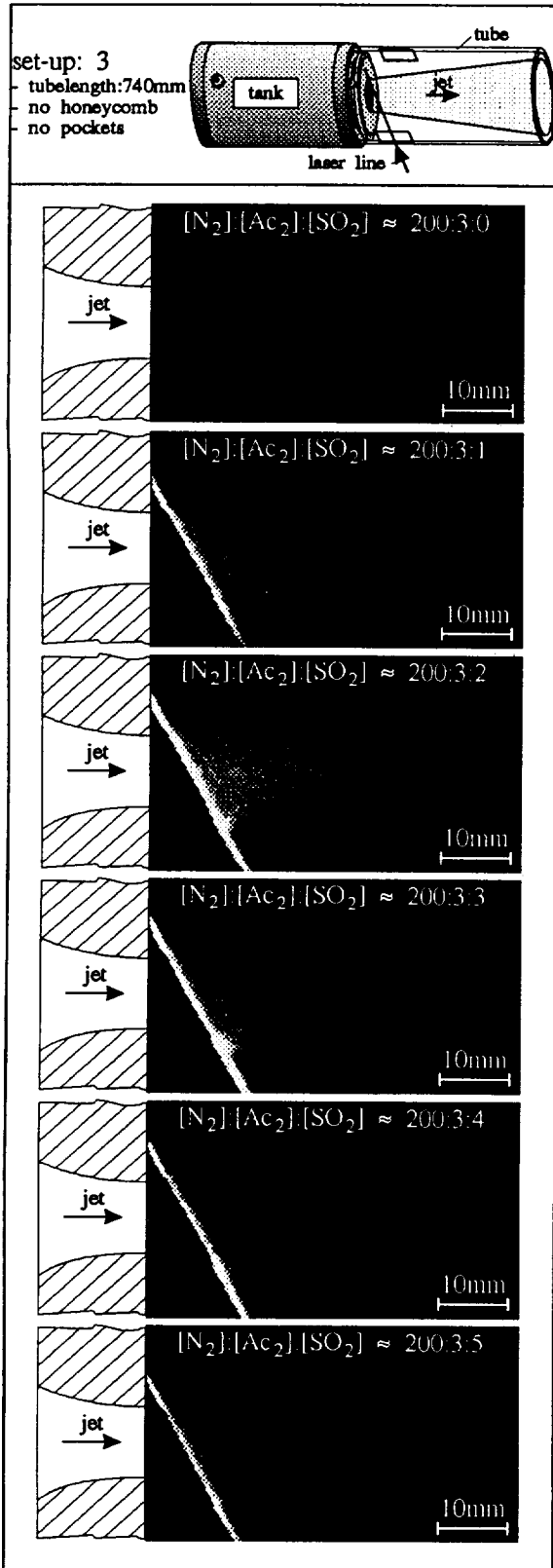Figure B2: Taken pictures for set-up 2
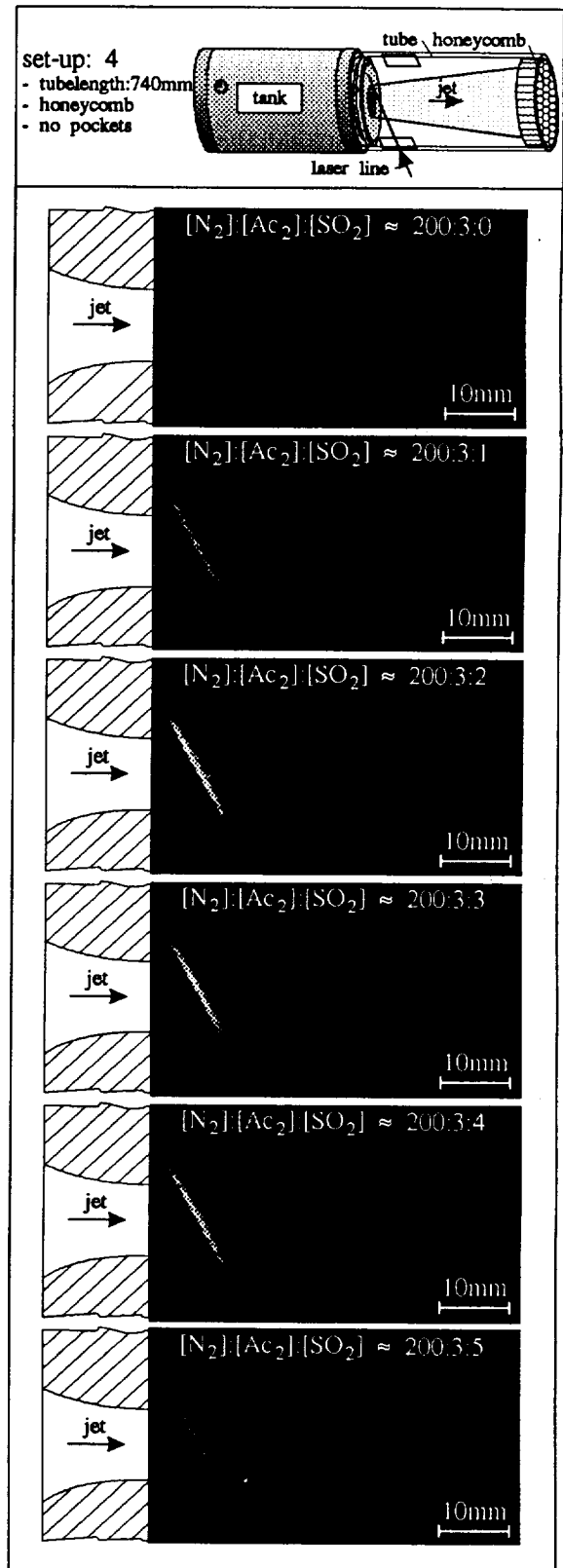
Figure B3: Taken pictures for set-up 3

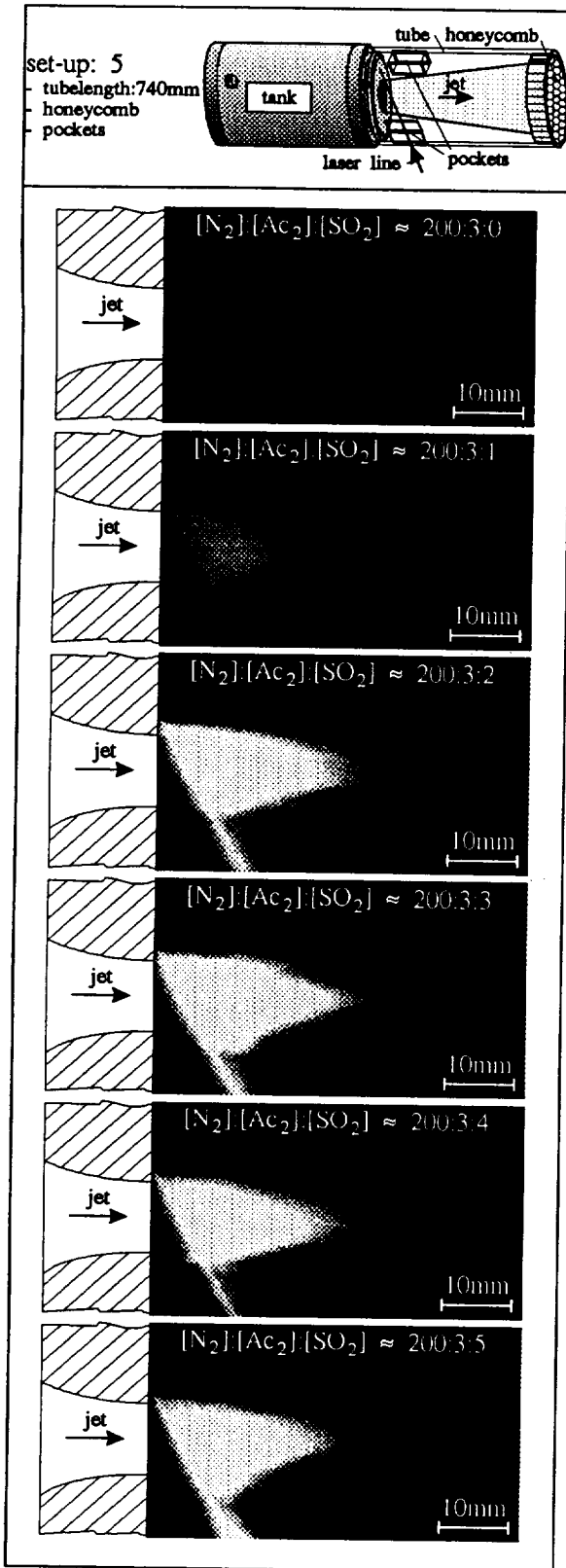Figure B4: Taken pictures for set-up 4

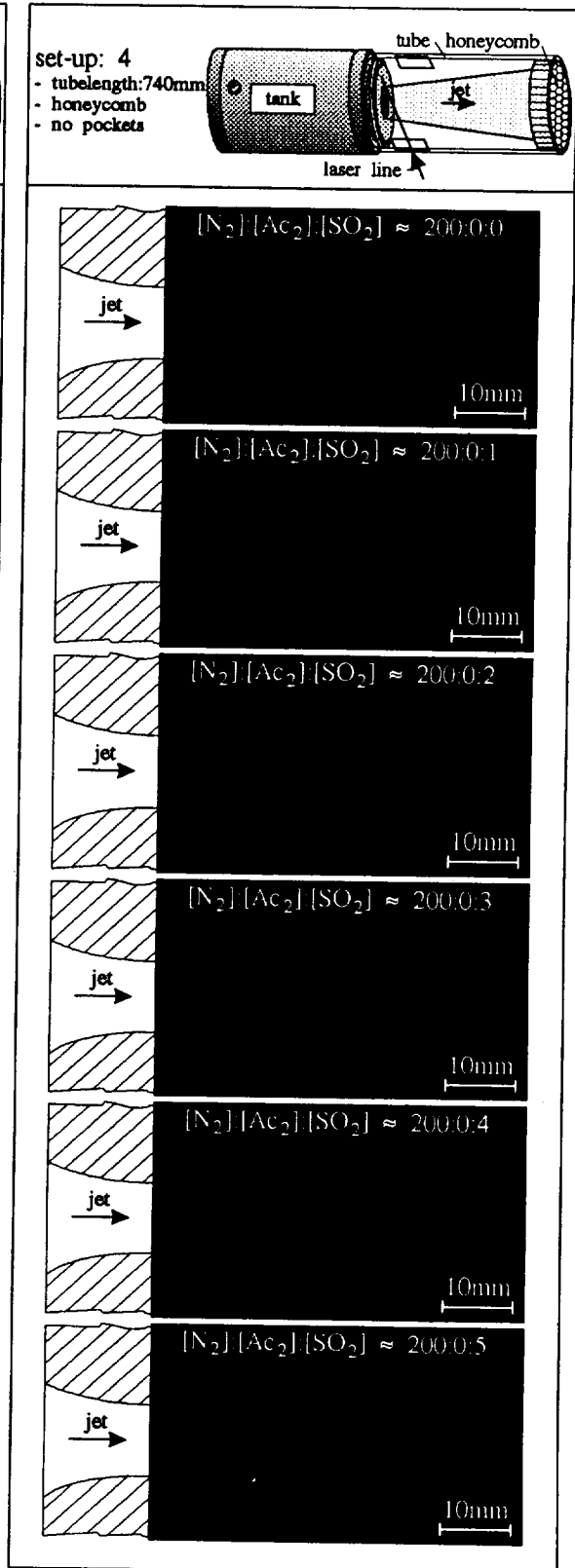Figure B5: Taken pictures for set-up 5

Figure B6: Taken pictures without biaceyl

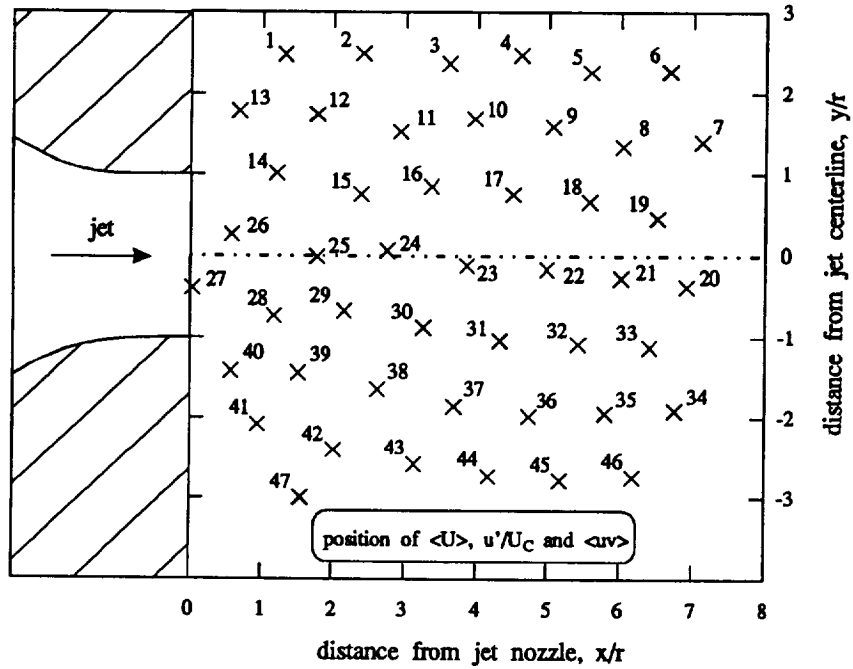## Appendix C: Data LIPA experiments

Figure C1: Numbering of the positions for mean velocity, turbulence intensity and Reynolds stress
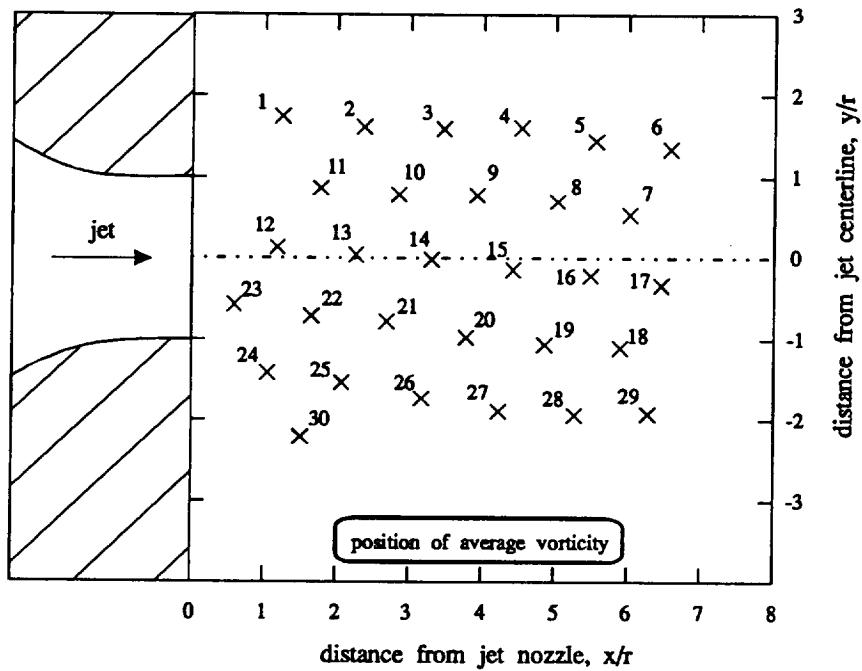

Figure C2: Numbering of the positions for mean vorticity

nr	position		velocity [m/s]			$(\delta<U_x>)_{rms}$ [m/s]	CR [m/s]	estimate [m/s]	
#	$<x/r>$	$<y/r>$	$<U_x>$	$<U_y>$	$<U>$		$(<U_{x,y}>)_{CR}$	area	$(U_{x_{estimate}}-<U_x>)$
1	1.29	2.50	-1.15	-3.32	3.93	1.60	0.25	A	-1.15
2	2.37	2.51	-0.49	-2.91	4.31	3.71	0.25	A	-0.49
3	3.58	2.38	-0.71	-1.00	2.72	1.74	0.25	A	-0.71
4	4.58	2.49	-1.99	-3.01	4.74	2.59	0.25	A	-1.99
5	5.56	2.28	-1.66	-1.43	3.76	2.20	0.25	A	-1.66
6	6.66	2.28	-1.68	-1.63	3.72	2.25	0.25	A	-1.68
7	7.10	1.41	4.03	0.89	6.10	4.53	0.25	M	-1.61
8	6.01	1.35	4.80	0.26	5.99	3.83	0.25	M	-0.78
9	5.04	1.60	3.96	0.43	5.03	3.14	0.25	M	2.57
10	3.93	1.70	1.40	0.31	3.28	2.15	0.25	A	1.40
11	2.90	1.54	1.40	0.18	3.35	2.35	0.25	A	1.40
12	1.74	1.76	1.63	-0.05	2.85	2.01	0.25	A	1.63
13	0.65	1.79	1.00	0.05	2.24	1.65	0.25	A	1.00
14	1.18	1.03	12.38	0.66	12.70	2.62	0.25	M	3.21
15	2.35	0.77	14.78	0.41	14.94	2.32	0.25	M	-1.02
16	3.34	0.86	13.15	0.00	13.32	3.26	0.25	M	-0.64
17	4.48	0.76	13.20	0.03	13.45	3.26	0.25	M	-1.27
18	5.55	0.67	13.30	-0.08	13.63	3.77	0.25	M	-1.58
19	6.49	0.46	12.48	0.28	12.73	2.87	0.25	M	-3.22
20	6.90	-0.37	12.38	0.08	12.62	1.99	0.25	M	-3.48
21	5.99	-0.27	14.68	-0.20	14.84	2.49	0.25	C	-1.28
22	4.96	-0.16	16.64	0.20	16.91	2.58	0.25	C	0.68
23	3.84	-0.11	17.26	-0.10	17.40	3.12	0.25	C	1.30
24	2.73	0.07	15.70	0.13	15.83	1.92	0.25	C	-0.26
25	1.74	0.00	16.16	0.00	16.32	1.62	0.25	C	0.20
26	0.55	0.26	16.41	0.03	16.53	2.09	0.25	C	0.45
27	0.00	-0.39	16.59	-0.26	16.61	1.22	0.25	C	0.63
28	1.15	-0.73	15.21	-0.23	15.39	1.37	0.25	C	-0.75
29	2.13	-0.67	14.98	-0.74	15.07	2.33	0.25	C	-0.98
30	3.22	-0.87	13.99	0.18	14.14	2.26	0.25	M	0.38
31	4.31	-1.04	13.27	-0.10	13.44	2.26	0.25	M	3.18
32	5.40	-1.08	12.15	0.03	12.36	2.76	0.25	M	2.61
33	6.39	-1.12	11.59	-0.64	11.89	2.95	0.25	M	2.42
34	6.74	-1.91	5.39	-0.56	7.34	3.55	0.25	M	4.79
35	5.78	-1.94	4.54	-0.38	5.66	2.91	0.25	M	4.52
36	4.72	-1.98	2.02	-0.84	4.09	3.11	0.25	A	2.02
37	3.67	-1.86	1.30	-0.43	3.11	2.47	0.25	A	1.30
38	2.59	-1.64	2.07	-0.23	3.57	2.65	0.25	A	2.07
39	1.49	-1.44	5.21	-0.77	5.80	2.13	0.25	A	5.21
40	0.55	-1.42	5.23	-0.87	6.15	2.77	0.25	A	5.23
41	0.92	-2.08	0.79	-0.36	2.72	1.97	0.25	A	0.79
42	1.99	-2.40	-0.79	0.05	2.34	1.50	0.25	A	-0.79
43	3.11	-2.58	-1.38	0.97	3.27	2.75	0.25	A	-1.38
44	4.15	-2.73	-1.43	1.89	3.64	2.26	0.25	A	-1.43
45	5.15	-2.79	-1.35	3.88	4.95	3.07	0.25	A	-1.35
46	6.16	-2.75	-1.89	1.84	3.90	2.83	0.25	A	-1.89
47	1.53	-3.00	1.30	3.06	4.34	2.93	0.25	A	1.30

Table C1: Velocities

nr	position		turbulent intensity [%]	$(\delta(u'/U_C))_{rms}$ [%]	RCR [%]
#	$\langle x/r \rangle$	$\langle y/r \rangle$	u'/U_C		$(u'/U_C)_{RCR}$
1	1.29	2.50	9.44	5.67	14.17
2	2.37	2.51	21.85	17.09	6.53
3	3.58	2.38	10.23	7.04	13.45
4	4.58	2.49	15.26	10.19	8.90
5	5.56	2.28	12.93	8.48	10.56
6	6.66	2.28	13.21	8.09	10.36
7	7.10	1.41	26.62	15.39	5.25
8	6.01	1.35	22.55	11.19	6.10
9	5.04	1.60	18.46	12.69	7.43
10	3.93	1.70	12.63	6.33	10.91
11	2.90	1.54	13.82	9.71	10.05
12	1.74	1.76	11.80	6.68	11.77
13	0.65	1.79	9.69	5.80	14.40
14	1.18	1.03	15.40	10.95	8.56
15	2.35	0.77	13.66	9.81	9.62
16	3.34	0.86	19.18	8.57	6.88
17	4.48	0.76	19.15	12.57	6.89
18	5.55	0.67	22.20	17.13	5.96
19	6.49	0.46	16.90	10.27	7.80
20	6.90	-0.37	11.72	7.68	11.21
21	5.99	-0.27	14.66	9.50	8.97
22	4.96	-0.16	15.17	8.81	8.66
23	3.84	-0.11	18.34	10.44	7.17
24	2.73	0.07	11.29	6.94	11.63
25	1.74	0.00	9.52	6.37	13.77
26	0.55	0.26	12.31	7.82	10.67
27	0.00	-0.39	7.20	4.52	18.21
28	1.15	-0.73	8.04	5.20	16.32
29	2.13	-0.67	13.68	10.33	9.60
30	3.22	-0.87	13.31	9.23	9.88
31	4.31	-1.04	13.27	7.39	9.91
32	5.40	-1.08	16.21	10.79	8.14
33	6.39	-1.12	17.37	10.68	7.60
34	6.74	-1.91	20.91	12.74	6.45
35	5.78	-1.94	17.12	10.44	7.90
36	4.72	-1.98	18.30	12.34	7.66
37	3.67	-1.86	14.50	10.55	9.72
38	2.59	-1.64	15.60	6.17	8.96
39	1.49	-1.44	12.53	8.55	10.63
40	0.55	-1.42	16.32	12.63	8.23
41	0.92	-2.08	11.61	7.54	12.01
42	1.99	-2.40	8.80	7.24	15.64
43	3.11	-2.58	16.16	10.82	8.80
44	4.15	-2.73	13.31	8.63	10.31
45	5.15	-2.79	18.05	14.87	7.60
46	6.16	-2.75	16.64	11.03	8.38
47	1.53	-3.00	17.23	11.43	8.03

Table C2: Turbulent intensities

nr	position		Reynolds stress $[m^2/s^2]$	$(\delta(<uv>))_{rms}$ $[m^2/s^2]$	RCR [%]
#	$<x/r>$	$<y/r>$	$<uv>$		$<uv>_{RCR}$
1	1.29	2.50	0.41	2.37	19.48
2	2.37	2.51	2.15	8.23	12.60
3	3.58	2.38	-1.26	3.15	16.29
4	4.58	2.49	-0.56	6.89	12.34
5	5.56	2.28	-3.58	6.91	12.95
6	6.66	2.28	-0.61	4.23	14.02
7	7.10	1.41	-6.17	11.13	9.52
8	6.01	1.35	-4.96	10.68	9.84
9	5.04	1.60	-2.67	9.31	10.52
10	3.93	1.70	-1.01	4.91	13.52
11	2.90	1.54	-0.92	4.56	11.95
12	1.74	1.76	0.80	2.15	16.06
13	0.65	1.79	-0.99	2.55	19.11
14	1.18	1.03	-0.27	5.92	11.56
15	2.35	0.77	-2.21	6.63	13.84
16	3.34	0.86	-1.24	7.05	11.93
17	4.48	0.76	-2.21	11.21	10.73
18	5.55	0.67	-6.72	12.22	9.33
19	6.49	0.46	-0.52	6.94	11.65
20	6.90	-0.37	0.63	5.13	14.45
21	5.99	-0.27	-1.29	5.90	13.53
22	4.96	-0.16	-1.80	8.13	11.20
23	3.84	-0.11	-1.80	8.29	12.32
24	2.73	0.07	-0.44	4.35	15.75
25	1.74	0.00	-0.72	4.03	16.70
26	0.55	0.26	1.11	4.67	15.65
27	0.00	-0.39	0.44	1.43	33.58
28	1.15	-0.73	0.79	4.21	18.98
29	2.13	-0.67	-0.92	2.83	17.94
30	3.22	-0.87	0.38	4.01	14.75
31	4.31	-1.04	0.04	5.39	14.62
32	5.40	-1.08	1.58	5.77	12.82
33	6.39	-1.12	-2.03	10.21	11.10
34	6.74	-1.91	10.17	36.42	7.26
35	5.78	-1.94	4.20	10.60	10.27
36	4.72	-1.98	-3.99	13.91	10.11
37	3.67	-1.86	-1.19	5.53	13.86
38	2.59	-1.64	0.24	8.64	11.69
39	1.49	-1.44	2.69	5.68	14.69
40	0.55	-1.42	5.28	11.21	11.22
41	0.92	-2.08	0.80	2.89	15.95
42	1.99	-2.40	0.81	2.30	18.25
43	3.11	-2.58	1.07	5.07	14.00
44	4.15	-2.73	3.80	8.35	12.85
45	5.15	-2.79	3.36	16.13	12.07
46	6.16	-2.75	0.99	5.74	13.15
47	1.53	-3.00	0.11	3.12	17.38

Table C3: Reynolds stress

| nr	position		vorticity [10/s]	$(\delta(<\omega_z>))_{rms}$ [10*1/s]	RCR [%]
#	$<x/r>$	$<y/r>$	$<\omega_z>$		$<\omega_z>_{RCR}$
1	1.22	1.77	179.91	72.09	8.94
2	2.34	1.65	171.38	79.96	7.22
3	3.44	1.62	191.58	75.93	8.28
4	4.51	1.64	176.34	84.52	7.55
5	5.54	1.47	177.90	92.78	6.19
6	6.57	1.38	168.41	84.03	6.43
7	6.01	0.56	129.94	90.68	2.82
8	5.01	0.72	142.01	82.18	2.71
9	3.90	0.80	174.44	71.99	2.84
10	2.83	0.81	183.87	64.53	2.83
11	1.75	0.89	160.70	62.89	2.84
12	1.16	0.14	33.86	49.68	2.14
13	2.24	0.04	2.97	62.94	2.09
14	3.28	-0.01	6.80	54.47	2.14
15	4.40	-0.14	5.30	51.14	2.14
16	5.47	-0.21	-24.61	70.37	2.26
17	6.44	-0.32	-6.20	69.82	2.51
18	5.89	-1.10	-134.25	66.12	2.97
19	4.84	-1.06	-160.39	72.88	2.89
20	3.76	-0.97	-185.82	54.58	2.79
21	2.67	-0.78	-140.78	43.35	2.73
22	1.63	-0.71	-165.87	69.68	2.48
23	0.56	-0.57	-129.34	57.74	2.40
24	1.03	-1.42	-211.86	96.60	4.77
25	2.05	-1.54	-176.43	52.36	5.87
26	3.15	-1.74	-184.13	61.34	7.89
27	4.21	-1.90	-180.98	70.70	8.32
28	5.26	-1.95	-142.32	94.64	7.19
29	6.27	-1.93	-167.58	149.18	6.43
30	1.49	-2.23	-56.62	66.63	18.52

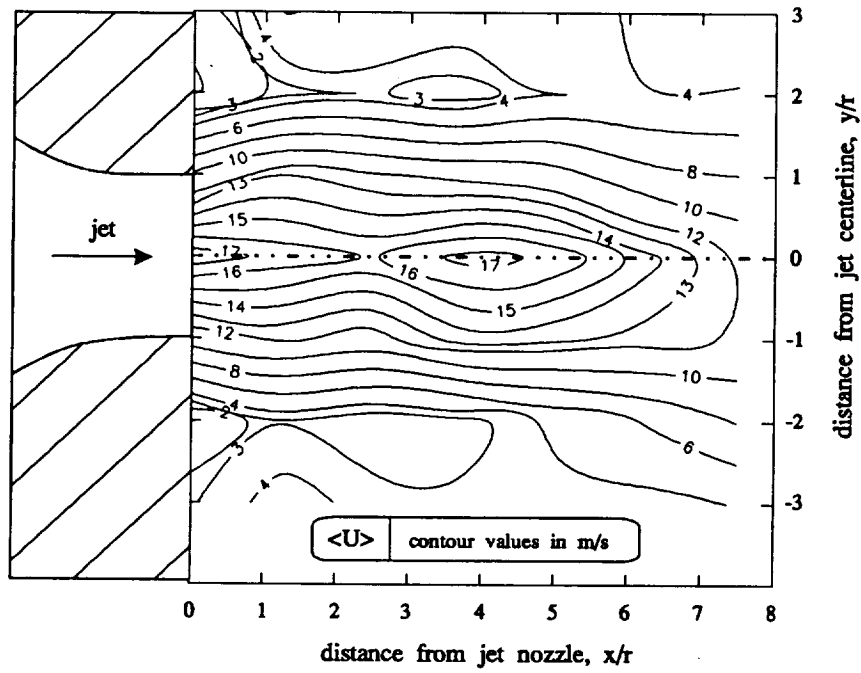Table C4: Vorticity
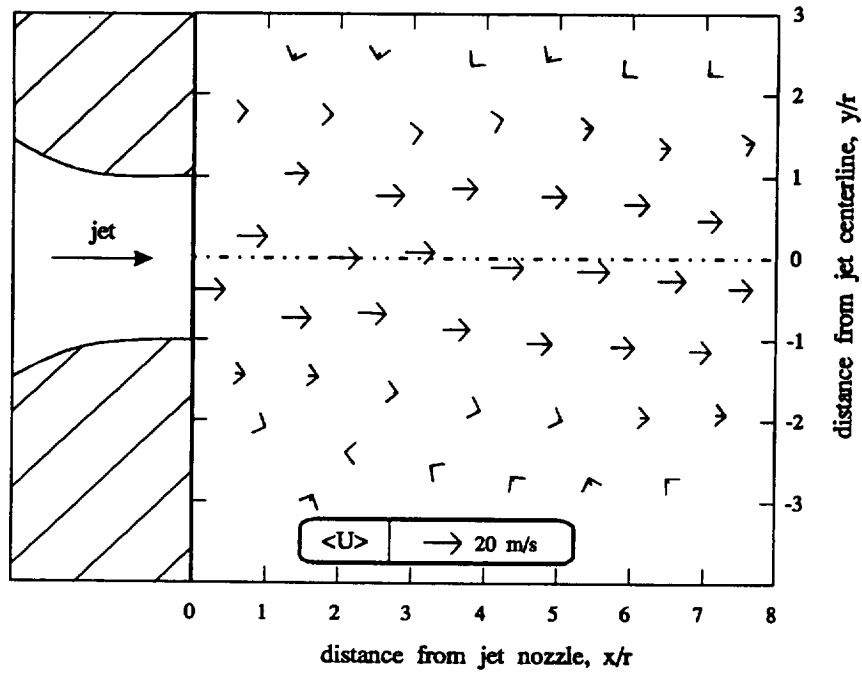
Figure C3: Velocity vectorplot
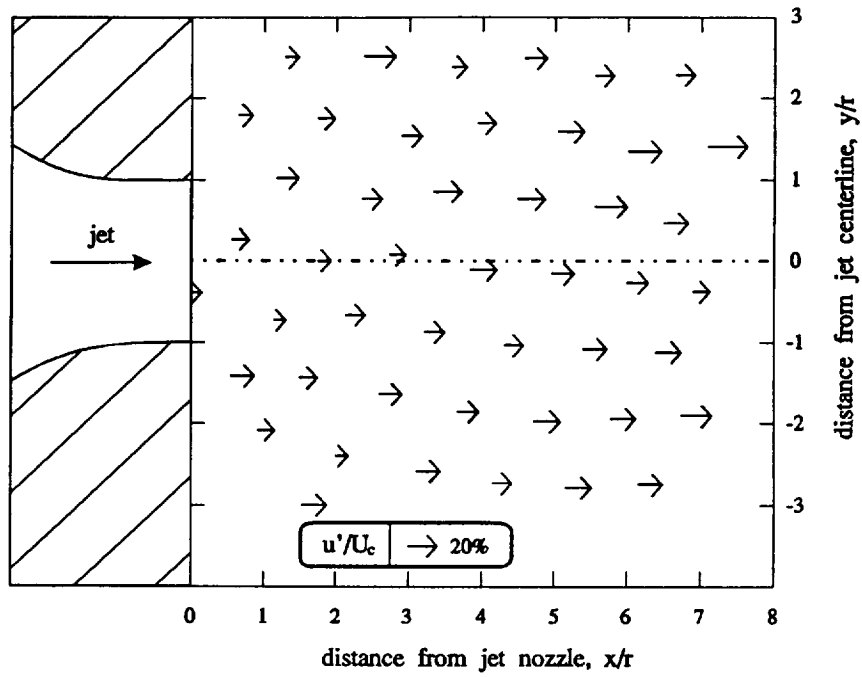

Figure C4: Velocity contourplot

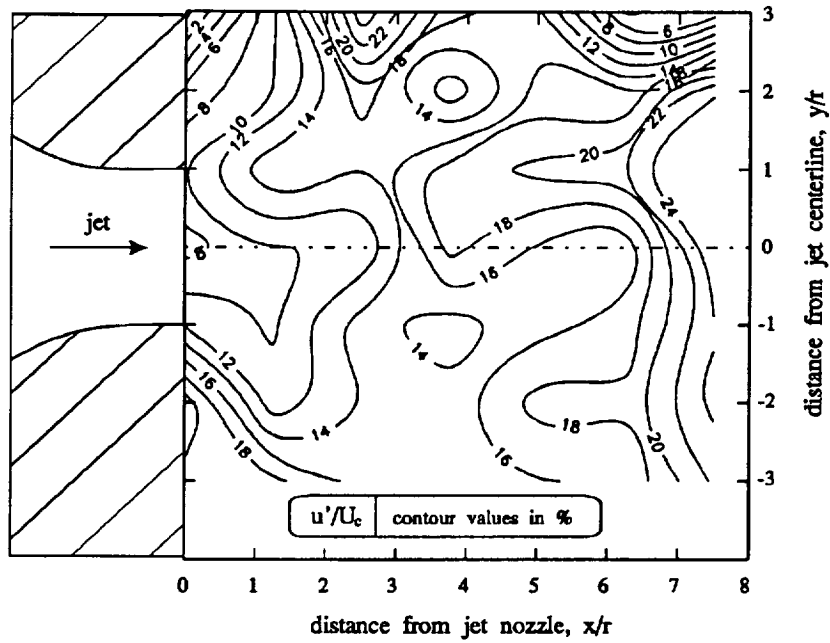Figure C5: Turbulent intensity vectorplot
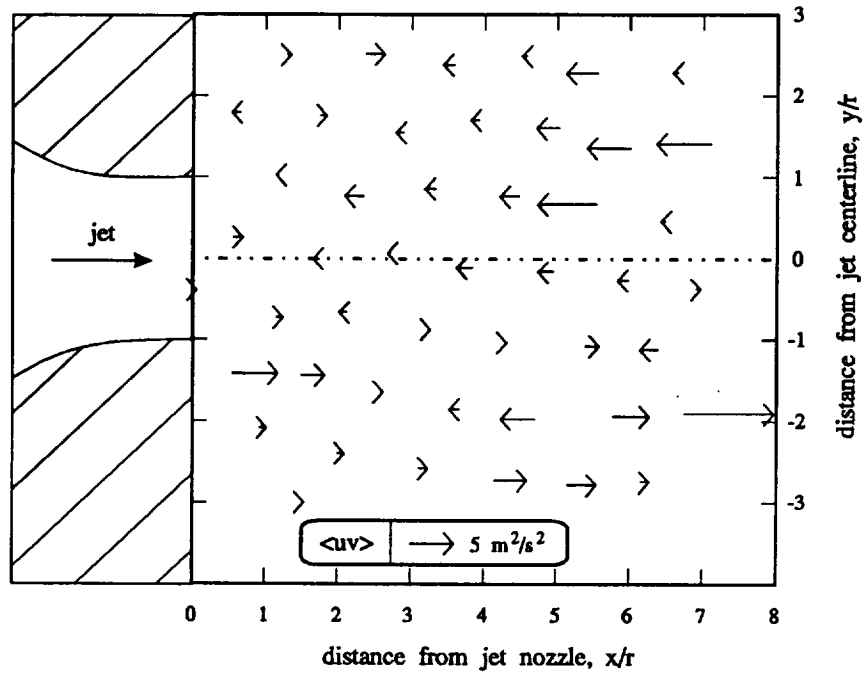

Figure C6: Turbulent intensity contourplot

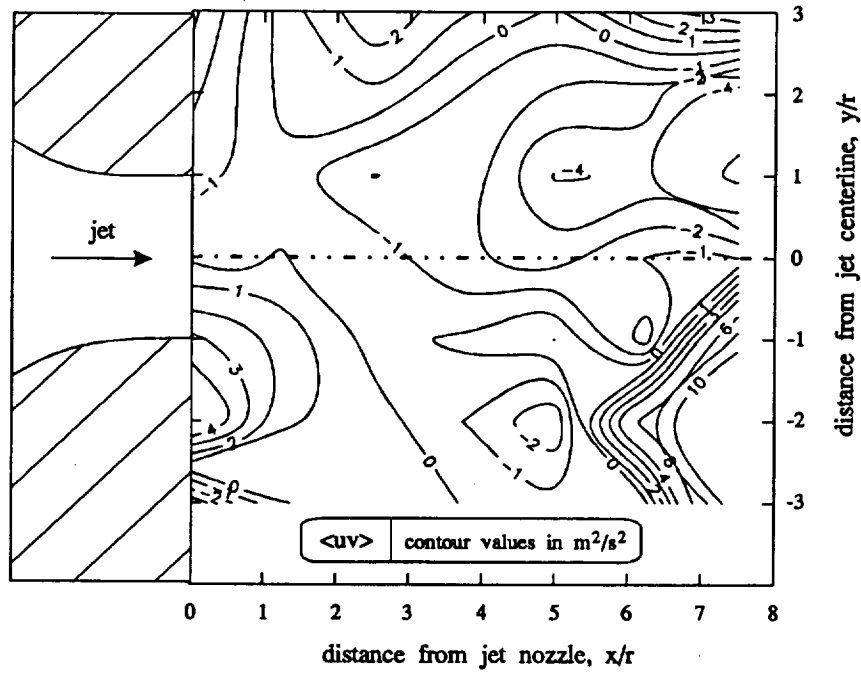Figure C7: Reynolds stress vectorplot
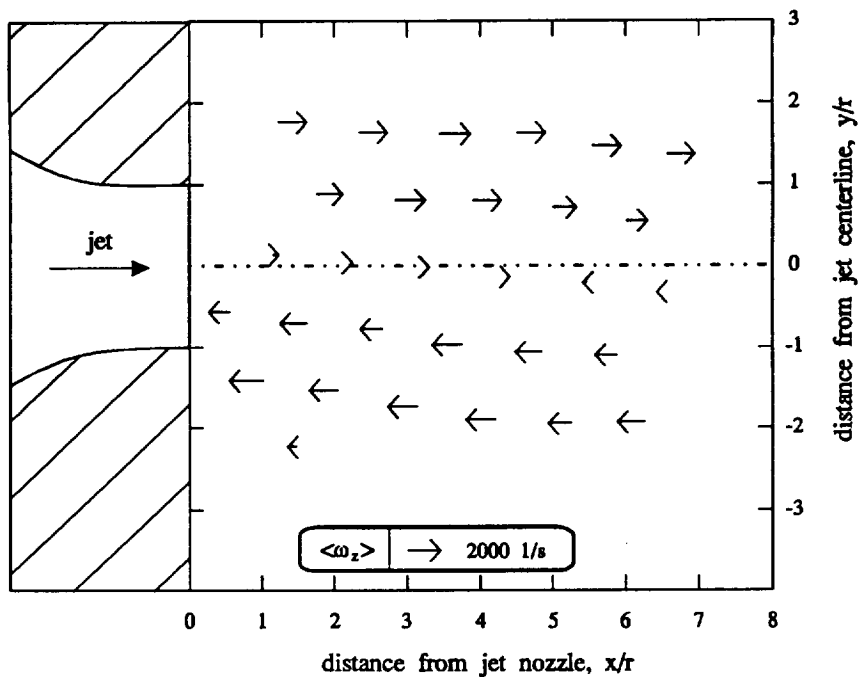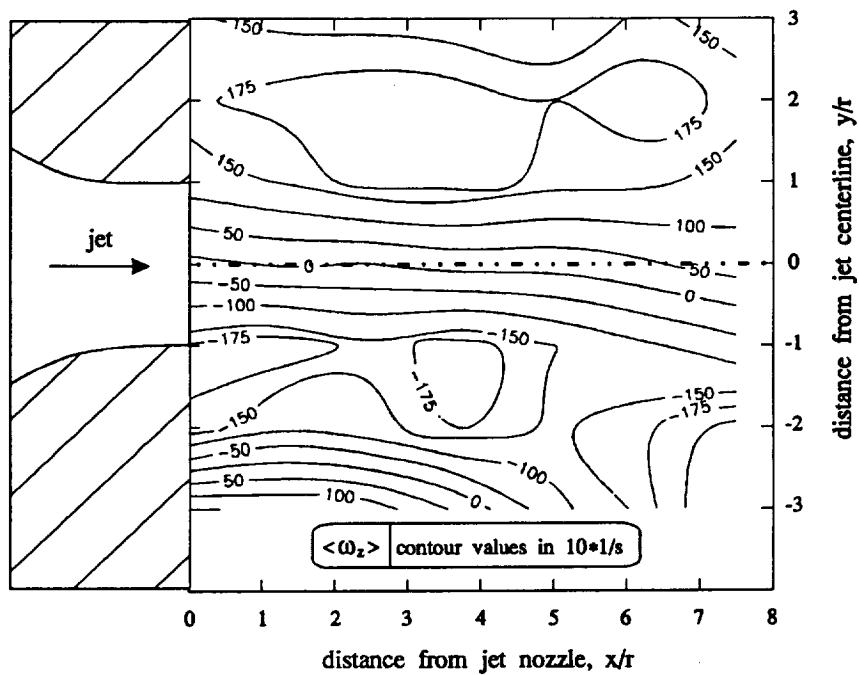

Figure C8: Reynolds stress contourplot

Figure C9: Vorticity vectorplot

Figure C10: Vorticity contourplot
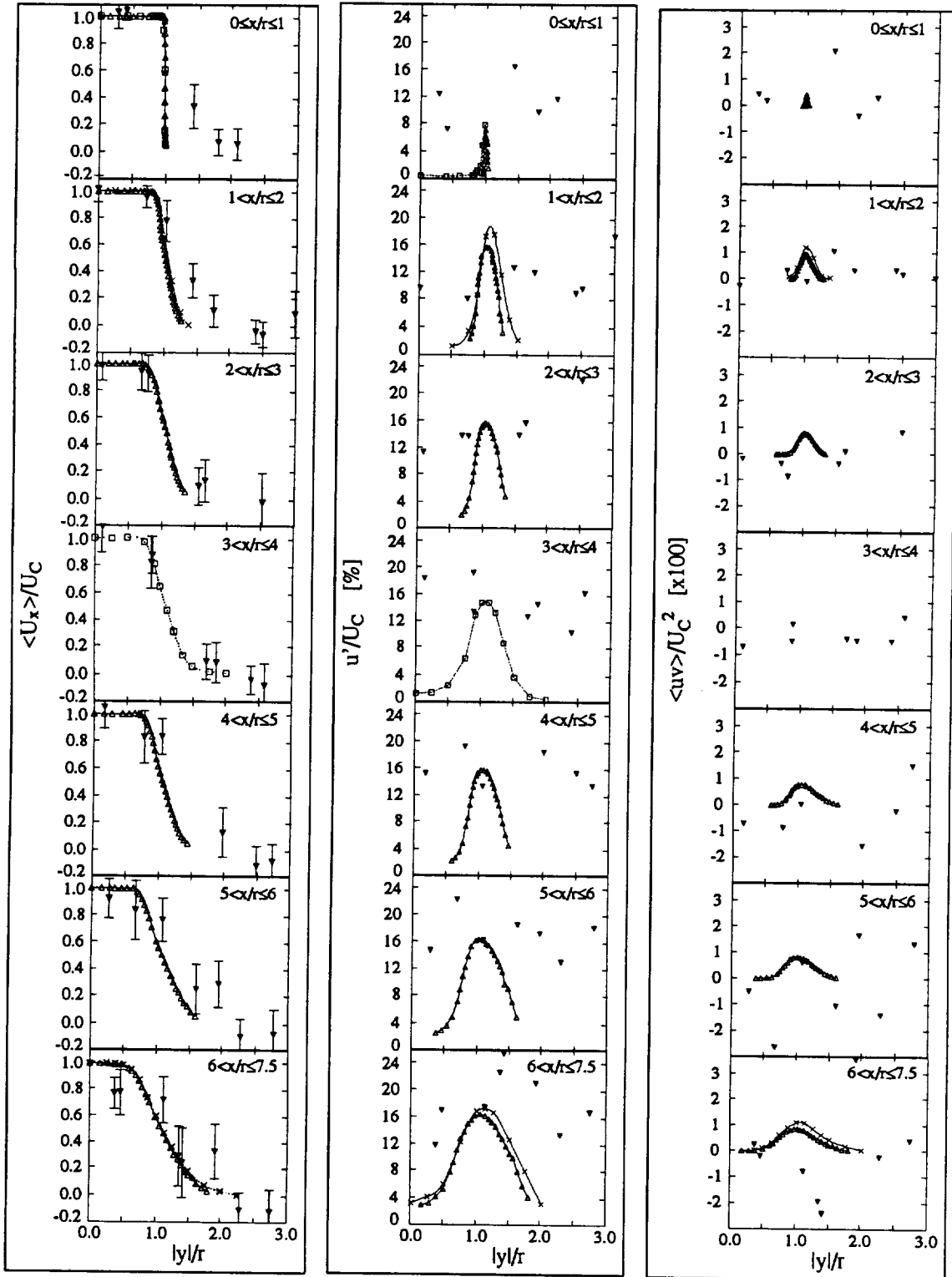
Figure C11: Comparison of performed measurments and data from the literature. ▼: here performed measurments; △ : measurments by Hussain and Clark [45] (Re_d=360000); □: measurments by Crow and Champagne [46] (Re_d=106000); ×:measurments by Sami, Carmody and Rouse [47] (Re_d=220000).
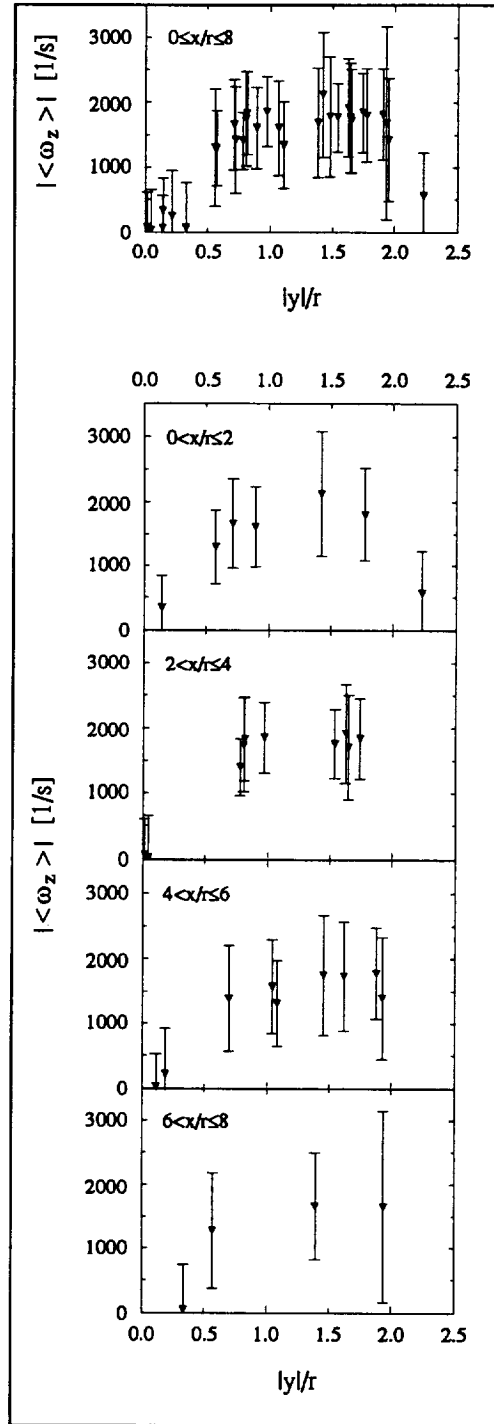
Figure C12: Plots of measured vorticity distribution for different intervals in flow direction.
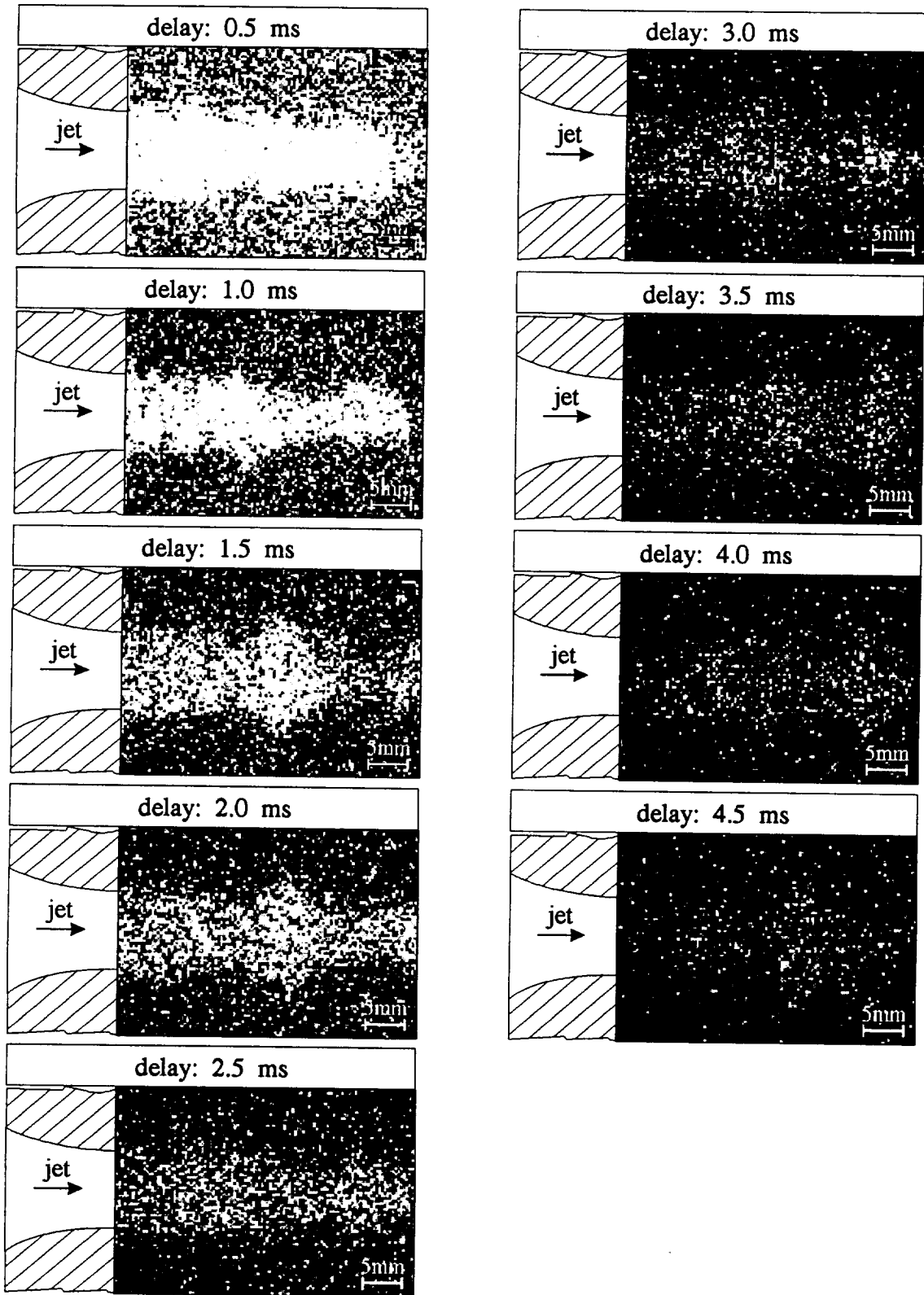
Appendix D: Lifetime experiments

Figure D1: Pictures taken with maximum intensification by the ICCD camera

Appendix E: Properties of chemicals

	N$_2$	SO$_2$	Biaceyl	O$_2$
M [g/mol]	28.013	64.06	86.06	31.999
R [J/(kg*K)]	297	127	95.6	260
ρ [kg/m^3]	1.161 (20° C; 1 atm)	2.717 (20° C; 1 atm)	979.23 (20° C; fluid state)	1.326 (20° C; 1 atm)
vapor pressure [kPa]			5.3 (20° C)	
c$_p$ [kJ/(kg*K)] (20° C)	1.038	0.640		0.917
c$_v$ [kJ/(kg*K)] (20° C)	0.741	0.504		0.656
κ	1.401	1.27		1.398

Table E1: Properties of chemicals [15,49,50,51]

(n-1)	required statistical safety [%]		
	95.0 %	99.0 %	99.9 %
1	12.71	63.66	636.62
2	4.30	9.93	31.60
3	3.18	5.84	12.94
4	2.78	4.60	8.61
5	2.57	4.03	6.86
6	2.45	3.71	5.96
7	2.37	3.50	5.41
8	2.31	3.36	5.04
9	2.26	3.25	4.78
10	2.23	3.17	4.59
20	2.09	2.85	3.85
30	2.04	2.75	3.65
40	2.03	2.71	3.55
50	2.01	2.68	3.50
60	2.00	2.66	3.46
70	1.99	2.65	3.44
80	1.99	2.64	3.42
90	1.99	2.63	3.40
100	1.98	2.63	3.39
200	1.97	2.60	3.34
300	1.97	2.59	3.32
400	1.97	2.59	3.32
500	1.97	2.59	3.31
1000	1.96	2.58	3.30
∞	1.96	2.58	3.29

Table E2: t-distribution as a function of number of measurements (n) and required statistical safety [16].